

Holography

Advanced Practical II



Tim Butcher - Florian Tönnies

Faculty for Mathematics and Physics
Albert-Ludwigs-Universität Freiburg

22nd February 2016

Abstract

During the course of the experiment several high precision holographic interferometry measurements were conducted. A test of the coherence of the used laser light (HeNe-laser) and the stability of the set-up with a Michelson interferometer was performed before the actual measurements took place. The elastic modulus of aluminium, brass and steel was extracted from the deflection of beams composed of these materials. The deflection of the beam was measured with the double-exposure technique of holographic interferometry. The results were:

Material	E_{Exp} / GPa	E_{Lit} / GPa
Aluminium	97 ± 9	72
Brass	115 ± 7	100
Steel	217 ± 15	195

These values are compatible with the literature value in a range of 3σ . The resonant frequencies of a fixed round aluminium plate were measured with the real-time technique:

mode	f / Hz
f_{00}	422
f_{10}	1068
f_{20}	1738
f_{11}	2931
f_{21}	4149
f_{31}	5429

The spacing of these frequencies follows the theoretical model. In the final part of the experiment the cross-correlation of two slits at different angles was analysed by Fourier interferometry. The theoretical predictions could be verified qualitatively.

Table of Contents

1	Introduction	3
1.1	Objective	3
1.2	Theoretical Background	3
1.2.1	Interference	3
1.2.2	Coherence	4
1.2.3	Diffraction	5
1.2.4	Fourier Optics	6
1.2.5	Basic Principle of Holography	10
1.2.6	Obtaining the reconstructed image	10
1.2.7	Types of Holograms	11
1.2.8	Holographic Interferometry	12
1.2.9	Workings of the experimental apparatus	13
2	Experimental Set-up and Procedure	16
2.1	Tasks	16
2.1.1	Michelson Interferometer	16
2.1.2	Double-exposure holography of metal beams under stress	17
2.1.3	Real-time holography of oscillating Aluminium plate	19
2.1.4	Fourier interferometry	20
3	Evaluation	21
3.1	Michelson Interferometer	21
3.2	Determination of the elastic moduli of the beam materials	21
3.3	Measurement of the resonant frequencies of the aluminium plate	27
3.4	Cross-correlation of two slits	32
4	Summary	35
4.1	Michelson Interferometer	35
4.2	Determination of the elastic moduli of the beam materials	35
4.3	Measurement of the resonant frequencies of the aluminium plate	36
4.4	Cross-correlation of two slits	36
5	Appendix	37
5.1	Calculation for the deflection of a beam	37
5.2	Resonant frequency of a fixed round plate calculations	38
5.3	Measured data	41
5.4	R Source code	51
6	List of Figures	55
7	List of Tables	56
8	Bibliography	57

1 Introduction

1.1 Objective

The first part of the experiment consists of the measurement of the elastic modulus of aluminium, brass and steel by holographic interferometry using a double exposure hologram. Prior to this the sensitivity of the optical table to external influences is to be tested with a Michelson-Interferometer. The second part deals with the real-time holography of a fixed plate in order to obtain its resonant frequencies. In the final part the cross-correlation function of two twisted slits is examined by Fourier interferometry.

1.2 Theoretical Background

1.2.1 Interference

The phenomenon of interference occurs when waves superpose, leading to a wave of a different amplitude. The interference of electromagnetic waves can be observed by measuring the intensity of the resulting superposition, which is given by the absolute square of the participating field amplitudes:

$$I = |E_{tot}(\vec{r}, t)|^2 = \left| \sum_j E_j(\vec{r}, t) \right|^2 \quad (1)$$

It is instructive to examine the interference of two plane waves ($E_1(\vec{r}) = E_{max_1} e^{-i(\vec{k}_1 \cdot \vec{r} + \delta_1)}$ and $E_2(\vec{r}) = E_{max_2} e^{-i(\vec{k}_2 \cdot \vec{r} + \delta_2)}$) with the same wavelength (Fig. 1.1). This implies that the absolute value of the wave vectors is identical ($|\vec{k}_1| = |\vec{k}_2| = k$), whereas the propagation directions need not be the same. The intensity at the position \vec{r} is given by:

$$\begin{aligned} I(\vec{r}) &= |E_1(\vec{r}) + E_2(\vec{r})|^2 \\ &= |E_1(\vec{r})|^2 + |E_2(\vec{r})|^2 + 2E_1(\vec{r}) \cdot E_2(\vec{r}) \cdot \Re[e^{-i(\vec{k}_1 \cdot \vec{r} + \delta_1)} \cdot e^{-i(\vec{k}_2 \cdot \vec{r} + \delta_2)}] \\ &= I_1(\vec{r}) + I_2(\vec{r}) + 2\sqrt{I_1(\vec{r}) \cdot I_2(\vec{r})} \cdot \underbrace{\cos((\vec{k}_1 - \vec{k}_2) \cdot \vec{r} + \delta_1 - \delta_2)}_{:= \Delta\phi(\vec{r})} \end{aligned}$$

Where the following relation was used:

$$E_1 E_2^* + E_1^* E_2 = E_1 E_2^* + (E_1 E_2^*)^* = 2\Re[E_1 E_2^*] \quad (2)$$

Using a trigonometric addition theorem and assuming that the constant phase factor equals zero ($\delta_1 - \delta_2 = 0$) one obtains the phase difference of:

$$\Delta\phi(\vec{r}) = kx \sin(\theta)$$

Which results in the formula for the two-beam interference intensity:

$$I(\vec{r}) = I_1(\vec{r}) + I_2(\vec{r}) + 2\sqrt{I_1(\vec{r}) \cdot I_2(\vec{r})} \cdot \cos(kx \sin(\theta)) \quad (3)$$

The waves are in phase when $\cos(\Delta\phi) = 1$ or $\Delta\phi = 2\pi n$ ($n \in \mathbb{N}$). This leads to maximum total intensity also known as *constructive interference*. Conversely *destructive interference* happens when

$\cos(\Delta\phi) = -1$ or $\Delta\phi = (2n + 1)\pi$ ($n \in \mathbb{N}$). This means that a stripy pattern will show up on a screen positioned at \vec{r} (neatly illustrated in Fig. (1.1), although this is a special case). The periodicity of the stripes is $\frac{\lambda}{\sin(\theta)}$.

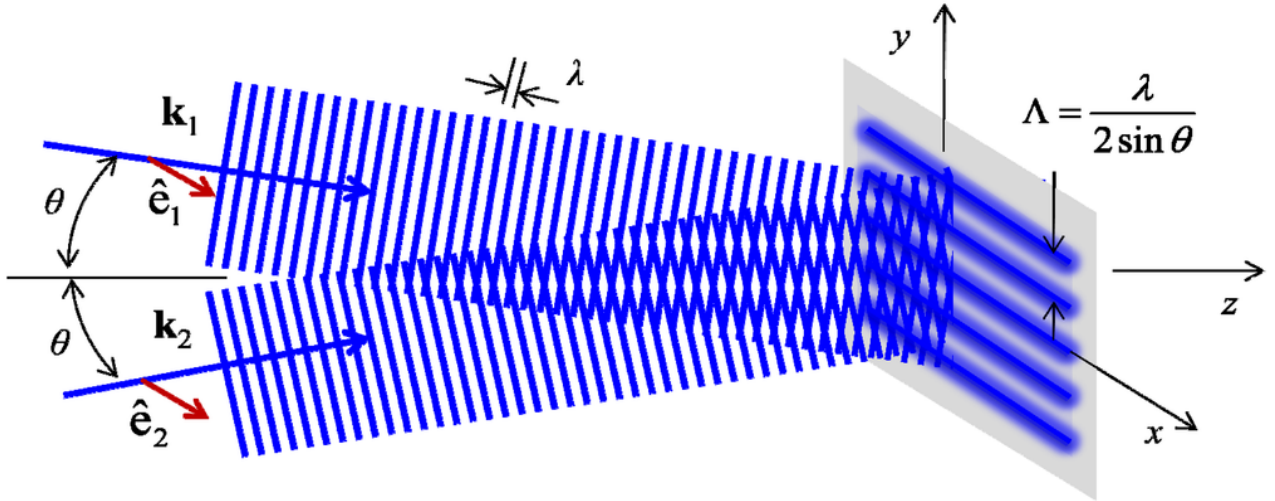


Figure 1.1: Interference pattern of two plane waves with wave vectors $\vec{k}_1 = -\vec{k}_2$ ¹

1.2.2 Coherence

The prerequisite for interference as described in the above section is that the light is coherent. The perfectly monochromatic and sinusoidal waves of the previous section can not be observed in reality. It can be said that interference is an indication of the coherence pertaining to a light source. The waves do not necessarily have to have the same phase in order to observe interference, although the contrast of the interference pattern decreases with higher phase difference. In the case of complete incoherence the $\cos(\Delta\phi)$ fluctuations become zero on average and the individual intensities simply add. A real light source emits wave packets of a specific length and bandwidth $\Delta\nu$. There are two types of coherence:

I. Temporal (longitudinal) coherence

A wave packet is temporally coherent when two measurements of the field in an interval of τ at the exact same position result in a constant phase relation:

$$\Delta\phi(t) = \phi(t) - \phi(t + \tau) = \text{const} \quad (4)$$

Due to the fact that the two measurements at t and $t + \tau$ are equivalent to measurements in longitudinal direction with a distance of $\Delta z = c\tau$ between them, *temporal coherence* is also known as *longitudinal coherence*. One way to measure temporal coherence is with a *Michelson interferometer* (see section 1.2.9). The *coherence time* (τ_c in formula 5) indicates the maximum time under which the wave packet may be considered temporally coherent (demonstrated in Fig. 1.2):

¹http://www.mdpi.com/micromachines/micromachines-02-00221/article_deploy/html/images/micromachines-02-00221f1-1024.png

$$\tau_c = \frac{1}{\Delta\nu} \approx \frac{\lambda^2}{c\Delta\lambda} \quad (5)$$

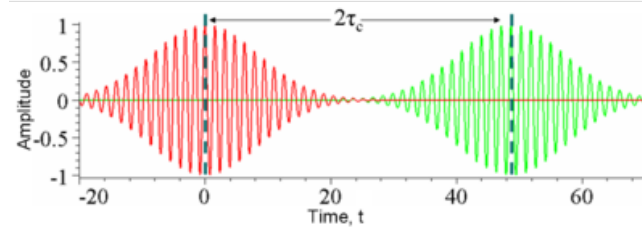


Figure 1.2: Coherence time τ_c of a wave packet ²

II. Spatial (transverse) coherence

A wave packet is spatially coherent if there is a constant phase relation between two positions which are shifted perpendicularly to the propagation direction (therefore *transverse*). The maximum phase difference that two coherent waves are allowed to exhibit is known as the *coherence length* (L_c). Spatial coherence can be measured with a *Young interferometer* (double slit). A plane wave has an infinite coherence length (Fig. 1.3). An example for a wave packet with finite coherence length can be seen in figure (1.4).

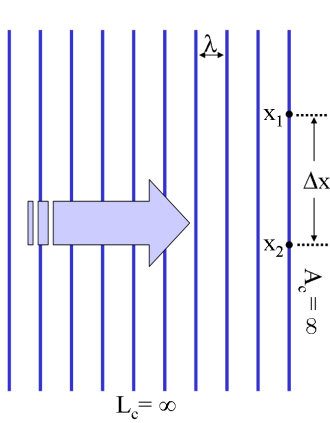


Figure 1.3: infinite coherence length L_c of plane wave³

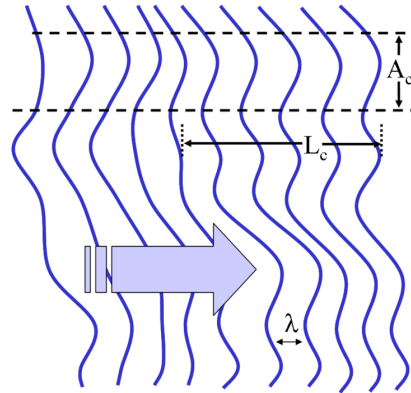


Figure 1.4: Wave packet with finite coherence length ⁴

1.2.3 Diffraction

When waves encounter an obstacle (or slit) the characteristic phenomenon that occurs is known as diffraction. In the figure below (1.5) the basic experimental setup (known as "Fraunhofer Arrangement") with which diffraction can be observed and which will be utilised in the experiment is shown.

²https://upload.wikimedia.org/wikipedia/commons/thumb/7/77/Wave_packets.png/400px-Wave_packets.png

³[https://en.wikipedia.org/wiki/Coherence_\(physics\)/media/File:Spatial_coherence_infinite_ex1.png](https://en.wikipedia.org/wiki/Coherence_(physics)/media/File:Spatial_coherence_infinite_ex1.png)

⁴[https://en.wikipedia.org/wiki/Coherence_\(physics\)/media/File:Spatial_coherence_finite.png](https://en.wikipedia.org/wiki/Coherence_(physics)/media/File:Spatial_coherence_finite.png)

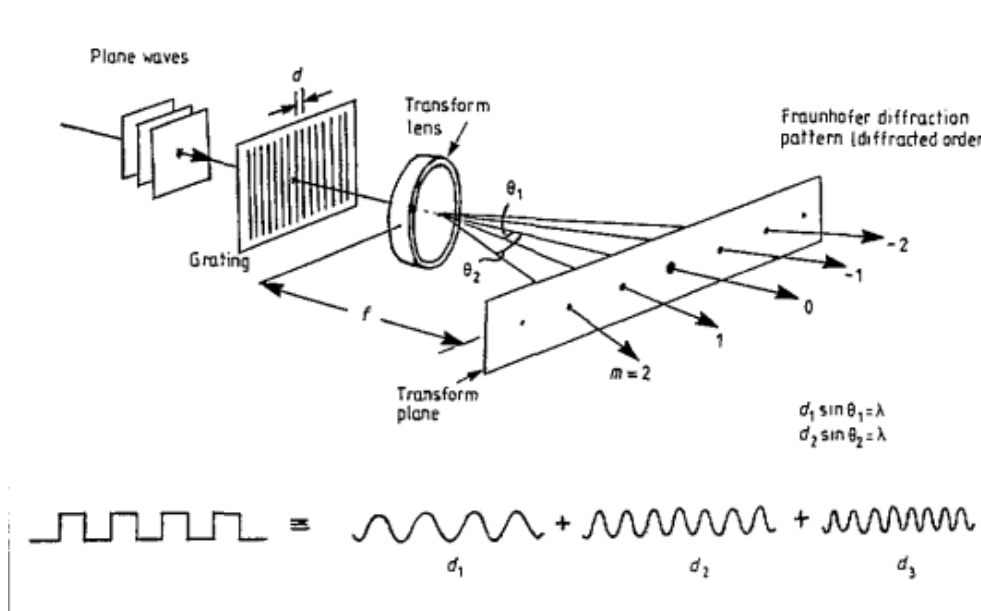


Figure 1.5: Schematic Fraunhofer Setup⁵

The parallel beams of light, to the left of the diffraction grating, originate from a collimator lens which has a distance of one focal length to the light source. Once the light hits the grating, it is diffracted. The reason for this is given by *Huygens Principle*: "Every unobstructed element of a wavefront acts as a source of spherical waves with the same frequency as the primary wave. The amplitude of the optical field beyond is a superposition of all these wavelets taking account of their amplitudes and phases." (from [4]). The constructive and destructive interference of these wavelets leads to the distinctive diffraction patterns. Whether the interference is constructive or destructive is governed by the optical path difference between the beams. The imaging lens projects the diffraction pattern onto a screen positioned at its back focal plane (the system of diffracting object-lens-screen is commonly referred to as a 2f-system, where the lens simply acts as a Fourier transformer). This means that the screen can be treated as being infinitely far away and makes the treatment of the diffraction as *Fraunhofer-Diffraction* viable. *Fraunhofer Diffraction* is ascertained if the electromagnetic field is examined in the *far field*. The position of the maxima and minima can be calculated by using geometric relations. Alternatively the *Fresnel-Kirchhoff Integral Formula*, which bestows quantitative expression upon *Huygens Principle*, provides a very elegant method of determining the diffraction pattern.

1.2.4 Fourier Optics

The *Fresnel-Kirchhoff Integral Formula* (6) describes the amplitude of a spherical wave on the edge of its propagation area. From this it follows that the field distribution of the light which has passed through a diffraction obstacle is given by the Fourier transform of the aperture function $g(x, y)$. The condition for Fraunhofer diffraction is that the observation distance $z \gg 1$.

$$U(x_0) = \frac{1}{\lambda z} C \mathcal{F}\{g(x, y)\} = \frac{1}{\lambda z} C \int_{-\infty}^{\infty} g(x, y) e^{-ikx} dx \quad C \cdot C^* = 1 \quad (6)$$

⁵<http://www.doitpoms.ac.uk/tplib/DD1-6/images/diagram11.png>

The aperture function is defined that it represents the amplitude and phase of the inbound wavefront hitting the obstacle. The intensity of the field distribution, which shows up on the screen, is given by the absolute square (the prefactors disappear due to normalisation):

$$I = |U(x_0)|^2 = \left| \int_{-\infty}^{\infty} g(x, y) e^{-ikx} dx \right|^2 \quad (7)$$

I. Single Slit

The aperture function of a single slit of length l and width b ($b \ll l$) is given by the *rect* (1.6) function defined by:

$$g(x) = \text{rect}\left(\frac{x}{b}\right) = \begin{cases} 1 & |x| \leq \frac{b}{2} \\ 0 & \text{otherwise} \end{cases} \quad (8)$$

The Fourier transform of which is the *sinc* (Fig. 1.6) function:

$$\mathcal{F}[g(x)] = |b| \cdot \text{sinc}\left(\frac{k \cdot b}{2}\right) = 2|b| \cdot \frac{\sin\left(\frac{k \cdot b}{2}\right)}{k \cdot b} \quad (9)$$

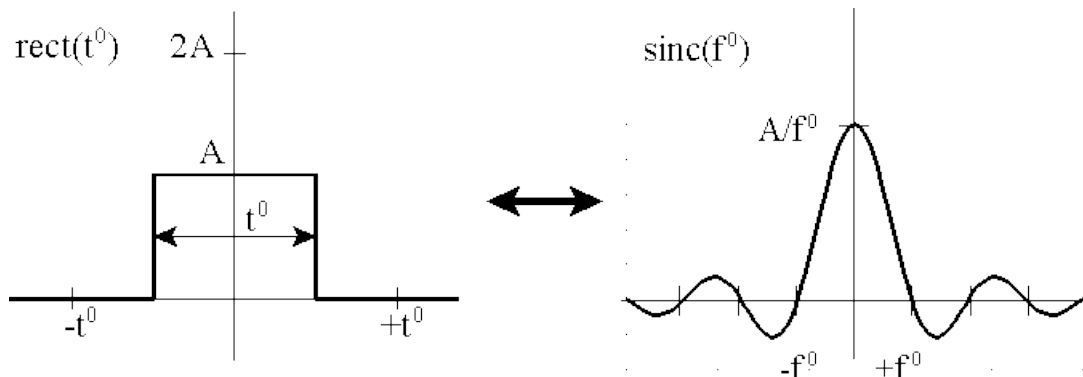


Figure 1.6: Fourier pair Rect/Sinc⁶

The intensity of the diffraction pattern is therefore:

$$I = |\mathcal{F}[g(x)]|^2 = \left(|b| \cdot \text{sinc}\left(\frac{k \cdot b}{2}\right) \right)^2 \quad (10)$$

⁶<https://www.chem.psu.edu/courses/chm621/text/ft/basiset/rect/rectangle.gif>

II. Convolution

The *convolution* of two functions is given by:

$$(f * g)(t) = \int_{-\infty}^{\infty} f(\tau)g(t - \tau)d\tau \quad (11)$$

This is the integral over the product of the original functions, as a function of the translation of one of the functions (given by the lag τ), which is inverted. The *cross-correlation* is very similar, only that the translated function is not reversed (the lag has a + instead of a - sign). If the two cross-correlated functions are identical, the process is known as *autocorrelation*. These three processes are illustrated in Fig. (1.7):

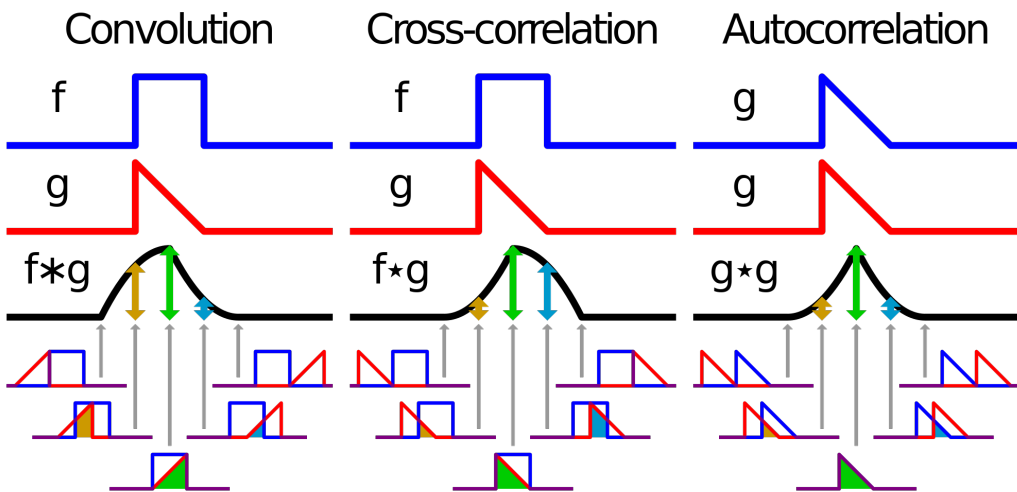


Figure 1.7: Visual comparison of convolution, cross-correlation and autocorrelation ⁷

In the figure one can see that convolution, cross-correlation and autocorrelation are maximised when the two participating functions match. Therefore they can be used to gain insight into the similarity of the two functions. For this reason the autocorrelation function can be spoken of as the *self-similarity function*.

A useful property of the Fourier transform goes by the name of the *convolution theorem*. It states that the convolution in position space corresponds to a multiplication in k-space, which is far easier to compute. The basic principle can be seen in Fig. (1.8).

⁷<https://en.wikipedia.org/wiki/Cross-correlation>

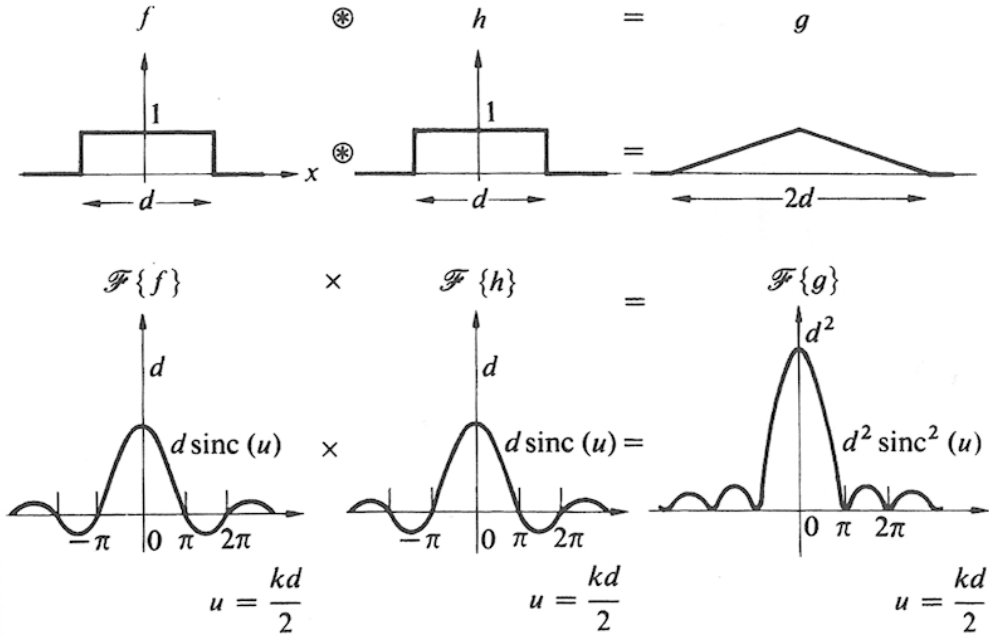


Figure 1.8: Illustration of the convolution theorem with the autocorrelation of the *rect* function ⁸

In Fourier optics the convolution (or cross-correlation) of geometrical forms can be achieved with a *4f-system* (Fig. 1.9). The front part of this is identical to a *2f-system*, where the first form is Fourier transformed. A multiplicative transmission mask (eg a spatial light modulator) is placed in the transform plane. This mask is encoded with the Fourier transform of the second function. Hence this is where the correlation takes place (as described by the *convolution theorem*). The correlation is made visible by performing a reverse Fourier transform with a further lens.

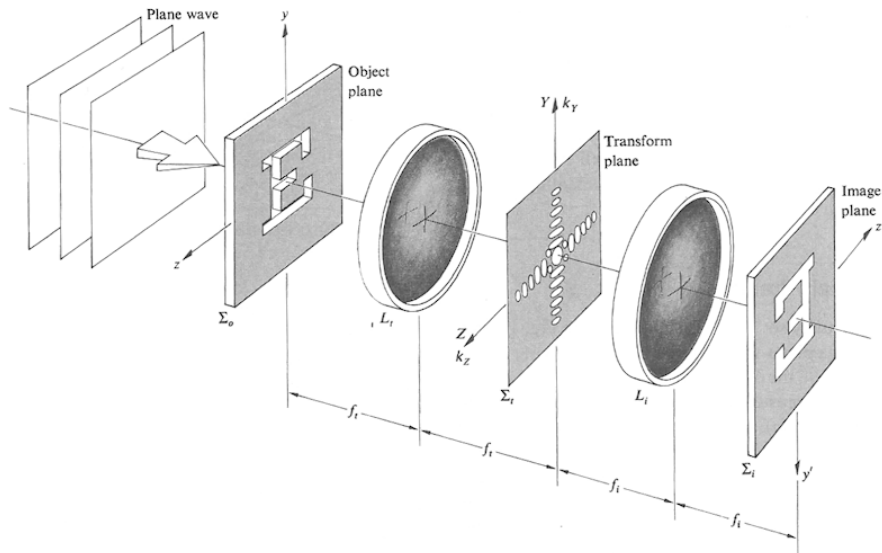


Figure 1.9: 4f-Correlator (with no mask in the transform plane) ⁹

⁸<http://www4.uwsp.edu/physastr/kmenning/images/Hecht4.11.F.26.png>

1.2.5 Basic Principle of Holography

Recording a hologram relies on the interference and diffraction of light waves. In addition holography is only possible with a light source that has a sufficient coherence. A laser (see section 1.2.9) satisfies this requirement. The basic set-up can be seen in Fig. (1.10). A laser beam is split in half with a beam splitter. One of the beams illuminates an object (*object beam*), while the other traverses the set-up unhindered (*reference beam*). Both beams are reunited on a photo plate, where they interfere, causing the characteristic intensity and phase information to be stored in the photo plate.

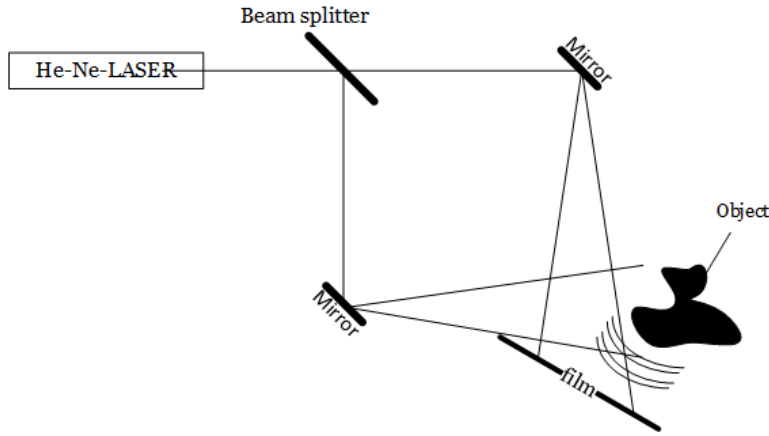


Figure 1.10: Setup for obtaining a hologram

It is possible to access this information later, by bringing the plate into contact with the original reference (reconstruction) beam (see below).

1.2.6 Obtaining the reconstructed image

The hologram acts as a spatial light modulator. Using the *Kirchhoff-Ansatz* for diffraction (equation 14) the field distribution can be calculated with the reconstruction beam ($A_R(\vec{r})$) and the *transmittance* (T_A) of the hologram.

$$A_R(\vec{r}) = A_R e^{ikx \sin \theta} \quad (12)$$

$$T_A = T_0 - C t_e I \quad (13)$$

Here t_e is the exposure time, I the intensity and T_0 and C are constants depending on the recording medium. Kirchhoff Ansatz and expanding gives the field distribution:

$$A(\vec{r}) = T_A A_R(\vec{r}) \quad (14)$$

$$= \underbrace{[T_0 - C t_E (I_1 + I_2) A_R e^{ikx \sin(\theta)}]}_{\text{no information}} - \underbrace{\sqrt{I_1 I_2} A_R C t_E e^{ikr}}_{\text{virtual image}} - \underbrace{\sqrt{I_1 I_2} A_R C t_E e^{-ikr} e^{2ikx \sin(\theta)}}_{\text{real image}} \quad (15)$$

The first term is simply the transmitted plane wave containing no information. The second term is proportional to the product of the original object wavefront and a linear exponential factor. This means that an outbound spherical wave with an angle of θ to the reconstruction beam is created by the diffraction. A virtual image of the object is observable. The third term stands for an inbound

⁹<http://www4.uwsp.edu/physastr/kmenning/images/Hecht4.13.F.31.png>

spherical wave converging to one point and creating a real image of the original object. The entire process is visualised in Fig. (1.11).

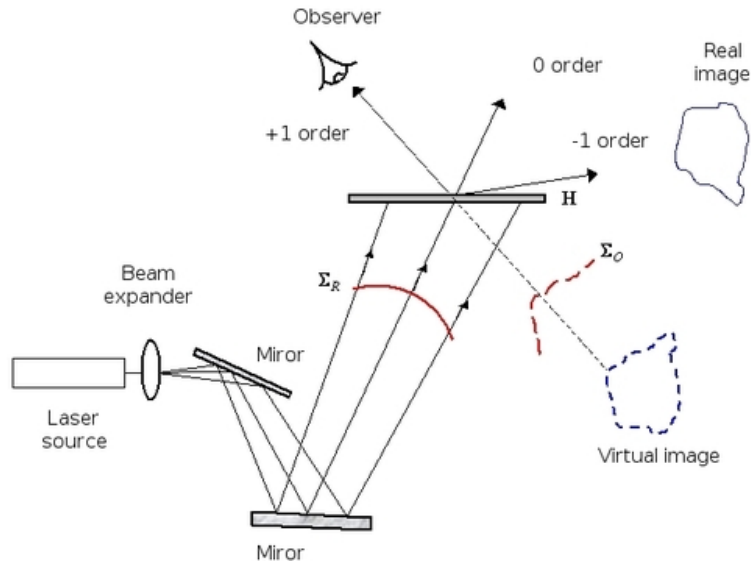


Figure 1.11: Setup for obtaining reconstructed images ¹⁰

1.2.7 Types of Holograms

I. Area and Volume holograms

If the depth of the recording medium is larger than multiple wavelengths a *volume hologram* is created. Otherwise one speaks of an *area hologram*. The special feature of a volume hologram is that a three dimensional lattice is formed in the recording medium. This in turn leads to *Bragg scattering* which means that the angle of reconstruction and reference beam must stay the same. The diffraction efficiency of a volume hologram is superior to that of an area hologram.

II. Amplitude- and Phase holograms

The treatment of amplitude- and phase holograms is equivalent to that of an amplitude and a phase grating. The amplitude hologram modulates the intensity of the inbound light, resulting in a non negligible loss of intensity of the holographic image. A phase hologram on the other hand modulates the phase of the inbound wave by a variable refractive index. This avoids the loss of intensity and has a higher diffraction efficiency.

III. Reflection- and Transmission holograms

Illuminating the photo plate by object- and reference wave from the same side results in a *transmission hologram*. If the sides differ one speaks of a *reflection hologram*. The direction in which the hologram must be looked at in order for a holographic image to be observed is governed by this.

¹⁰http://www.optique-ingénieur.org/en/courses/OPI_ang_M02_C10/res/Fig_08.jpg

1.2.8 Holographic Interferometry

A very precise way of analysing microscopic displacements is *holographic interferometry*. There are a number of different holographic interferometrical techniques:

I. Double-Exposure Method

The *double exposure method* consists of recording two holograms of the different states of the object on the same photo plate. The exposure time of each state is halved. The interference of the light of the two states can then be analysed with the reconstruction beam. One is then able to gather information required for the comparison of the states of the object by analysis of the pattern.

II. Time-Average Method

It is also possible to record a hologram of a moving object. A multitude of object states can be captured in the photo plate and accessed at the same time after the development process. As this is equivalent to taking the average over the phases corresponding to the states of the object, this is referred to as the *time-average method*.

III. Real-Time Method

In the *real-time method* a hologram of one specific state of the object is recorded. This hologram is then positioned back at the same position where it was recorded. By doing this it is possible to look at the hologram and the original object at the same time. Movement of the original object causes an interference pattern to appear on it. From this one is able to gain insight into the movement of the object.

1.2.9 Workings of the experimental apparatus

I. Helium-Neon Laser

A helium-neon laser consists of a gas discharge tube, containing a mixture of helium (for pumping) and neon (the actual laser medium), and a resonator. The gas discharge is triggered by an applied current. Electron collisions cause an excitation of helium and neon atoms. Helium has two metastable states (2^1S_0 and 2^3S_1 see Fig. 1.12) for which the transition to lower energy levels through the emission of dipole radiation is forbidden. These have long-lived population. The helium atoms in these states collide with the neon atoms resulting in the occupation of the $5S$ and $4S$ states of neon. This eventually leads to an occupation inversion between the higher lower states. This is because the energetically lower states decay very quickly under spontaneous emission. Visible coherent laser light is emitted at a wavelength of 632.8 nm (characteristic red light).

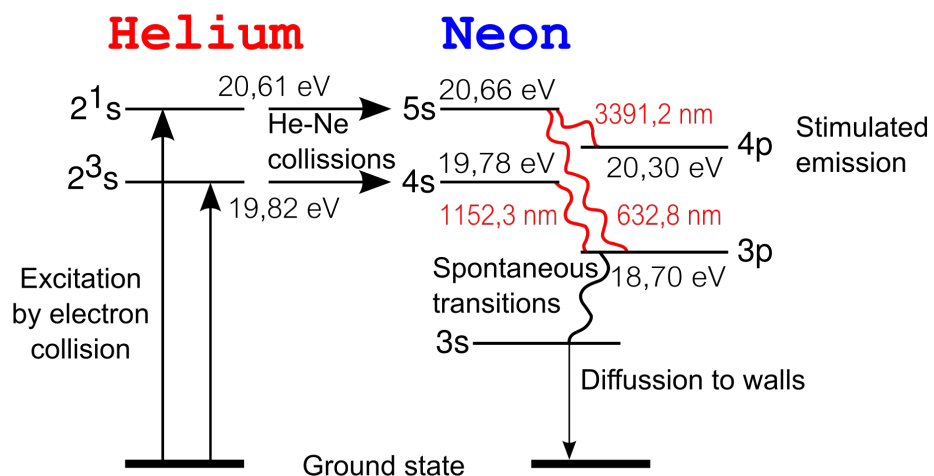


Figure 1.12: Term diagram of a He-Ne-Lasers¹¹

II. Michelson interferometer

A Michelson interferometer is commonly used to examine the temporal coherence of a light source. The emitted light (in this case from HeNe-laser) encounters a beam splitter and the two resulting beams (1 and 2 in Fig. 1.13) propagate independently to one another. After a specified length (L_1 and L_2) they are reflected by mirrors and recombine in the beam splitter. The optical path difference between the two paths results in the appearance of an interference pattern on the screen. The interference pattern is no longer observable if the coherence of the light is not ensured. The coherence can be impinged by introducing refracting objects or increasing the length of one arms.

¹¹https://en.wikipedia.org/wiki/Helium-neon_laser/media/File:Hene-2.png

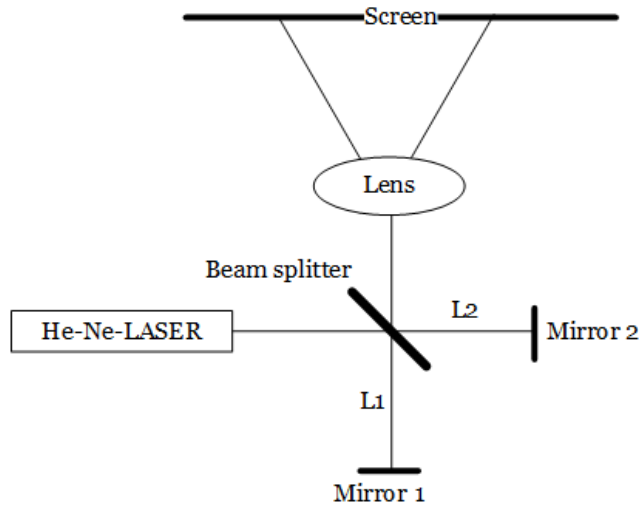


Figure 1.13: Path of light in a Michelson interferometer

III. Spatial filters

Spatial filters fulfil two purposes. They cleanse the laser light of disturbing effects caused by impurities in the optics, diffraction by dust particles (see Fig. 1.15) or variations in the laser gain medium itself. On the other hand they transform the incoming light into a spherical wavefront (if the second lens is omitted). A spatial filter consists of a collecting lens with a very small focal length (in the experiment the ocular of a microscope is used $f \approx 4\text{ mm}$). This lens performs a Fourier transform of the inbound light. The obtained Fourier transform in the focal plane resembles an *Airy pattern* (Fig. 1.14). By placing a tiny aperture (*pinhole*) in the focal plane one is able to effectively remove all unwanted higher spatial frequencies and only let the bright central spot pass. The resulting light has a very smooth transverse intensity profile and behaves like a spherical wave.

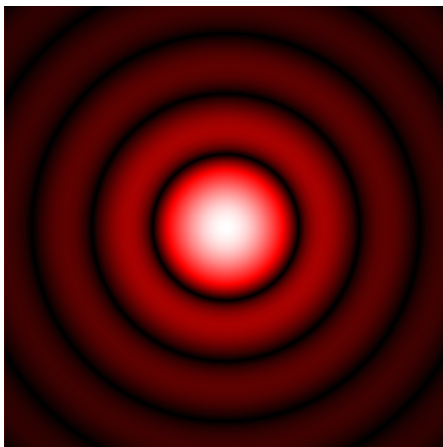


Figure 1.14: Airy disk (outer rings brightened)

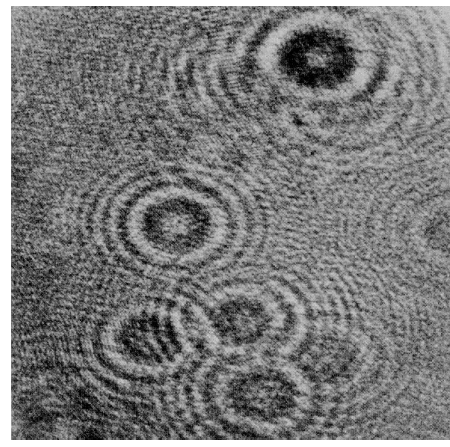


Figure 1.15: Polluted widened beam caused by dust particles ¹²

¹²<http://mb-s1.upb.de/LTM/EMM/Themen20und20Inhalte20der20Experimentellen20Mechanik/0ptische20Methoden/Holografie/Holografie.PDF>

IV. Holographic recording medium

The most common recording medium for Holography are silver halide layers. Because of the small size of these crystals the achievable resolution is far higher than in conventional photography (the angular resolution is ca 5000 lines/mm [2]). The crystals (usually silver bromide AgBr) are placed in a gel with a thickness of several micrometers which is spread on glass or film. The sensitivity of the layer to specific wavelengths is ensured through the usage of certain additives (organic dyes). Exposure to light induces a photochemical reaction in which the silver and the bromine atoms are separated. However the exposure time required in order to split the entire silver bromide is far too long. It is possible to shorten the exposure time (by a factor 10^6 [2]) which only produces individual Ag atoms in the AgBr corns. During the development of the photo plate the silver atoms act as a catalyst completely transforming the exposed corn to silver. The silver atoms absorb light blackening the exposed layer while the places that were left unexposed (due to interference) remain transparent. Hence an amplitude hologram has been created. The rest of the AgBr will eventually decompose, effectively rendering the hologram useless. The AgBr is removed by bleaching the photo plate. After the bleaching process a phase hologram is obtained.

V. Pockels cell

Applying an electric field to a crystal with no inversion symmetry produces birefringence. This effect is known as the *Pockels effect* (also known as the linear electro-optic effect). The real-time hologram of the aluminium plate relies on Pockels cells which utilise the Pockels effect. With these the polarisation of a light beam that pass through the cell can be changed. The combination of the cell with a polariser enables an extremely fast gate for the light beam, by switching between no rotation and a 90° rotation of the polarisation plane.

2 Experimental Set-up and Procedure

2.1 Tasks

1. The sensitivity of the optical bench to external influence is to be tested with a Michelson-interferometer and the coherence properties of the laser are to be investigated.
2. The deflection of three beams (clamped at one end and made of aluminium, brass and steel) due to strain with a very minute force is to be examined. This is to be accomplished by recording a double-exposure hologram of the beams under strain and relaxed. The elastic moduli of the beams are to be determined from the positions of the minima in the resulting interference pattern.
3. The resonant frequencies of a fixed round aluminium plate are to be determined by real-time holography.
4. The cross-correlation function of two rotated slits is to be analysed by Fourier interferometry.

2.1.1 Michelson Interferometer

A Michelson interferometer was set up as described in **1.2.9**. Figure **2.1** shows the final set-up.

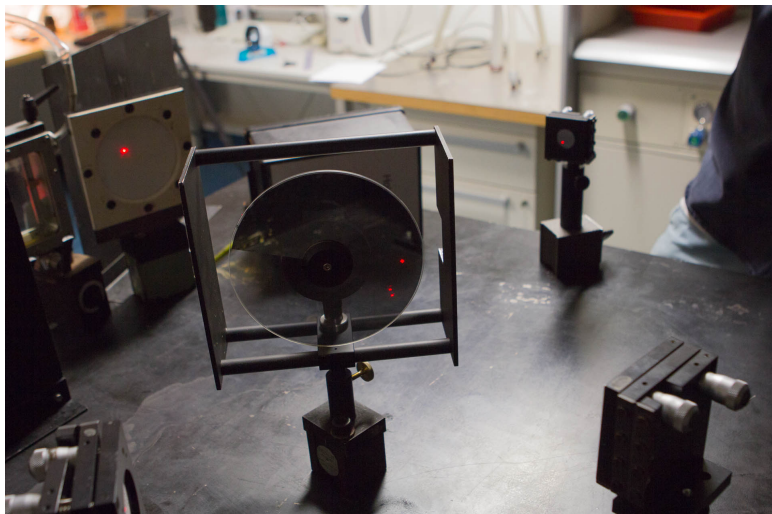


Figure 2.1: Experimental set-up Michelson interferometer

A beam splitter disc was used instead of a beam splitter cube. As the laser beams in the arms of the interferometer were not widened, the laser dots had to overlap completely for the interference pattern. This was rather easily achieved with the fine screws of the mirror. The lengths of the arms of the interferometer were measured with a tape measure. The stability of the interference pattern was tested by disturbing the set-up in number a of different ways (see section 3.1).

2.1.2 Double-exposure holography of metal beams under stress

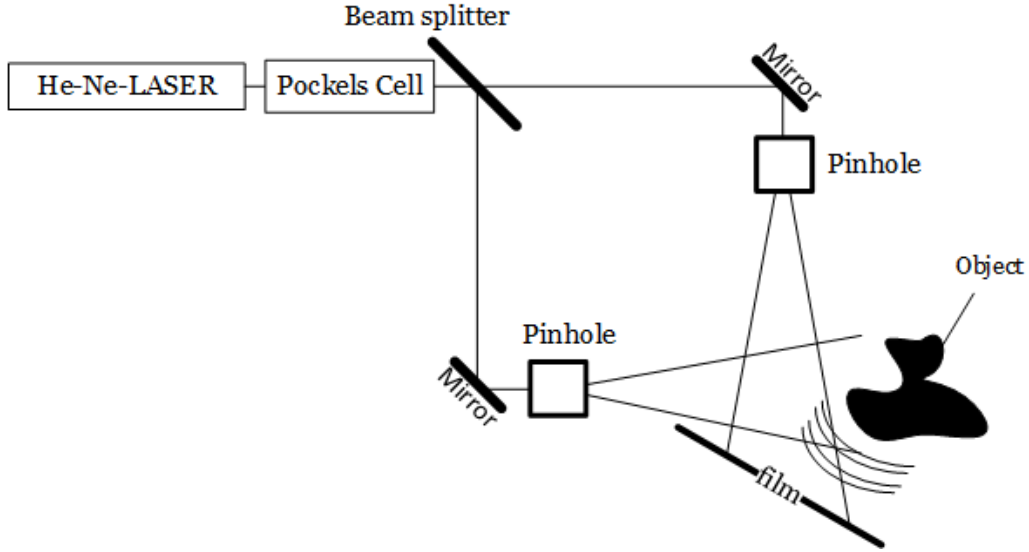


Figure 2.2: Experimental set-up used in part 2 and 3

The set-up used for the double-exposure holography and the real-time holography is shown in Fig. 2.2. The beam splitter disc was used to separate reference and object beam. The intensity of these beams (relative to each other) could be adjusted by turning the disc, because the coating intensity was varied. The intensity of the reference beam should ideally be ten times as high as that of the object beam. As the photo diode, with which the intensity was supposed to be measured proved to be highly unreliable, the correct configuration of the beam splitter was estimated. Pinholes were placed behind the mirrors to ensure clear and widened beams. The glass plate holding the photographic film was placed at around about 56° (Brewster angle) to the reference beam to slightly reduce the interfering reflection.

After this the room was darkened and the hologram was recorded. The following time intervals for the recording of the hologram were chosen (more or less by trial and error):

Exposure time : $2 \times 40\text{ s}$

Development time = 3 min

The photographic film was bleached until the colouration had almost disappeared. The finished hologram was placed back between the glass plates and illuminated by the reference beam. The angles between the metal beams, illumination and observation direction were measured with a set square (see Fig. 3.2 in section 3.2). By looking through the hologram one could see a stripy interference pattern on the metal beams (see Fig. 2.3). Finally the distance between the minima of the interference pattern and the clamping point of the beams were measured with a ruler. As measuring the distances by eye proved to be rather error prone, a different technique was used. A photograph of the beams with interference pattern and with a ruler was taken (the camera was fixed with a tripod). The two photographs were then fitted together with Adobe Photoshop (see Fig. 2.4).

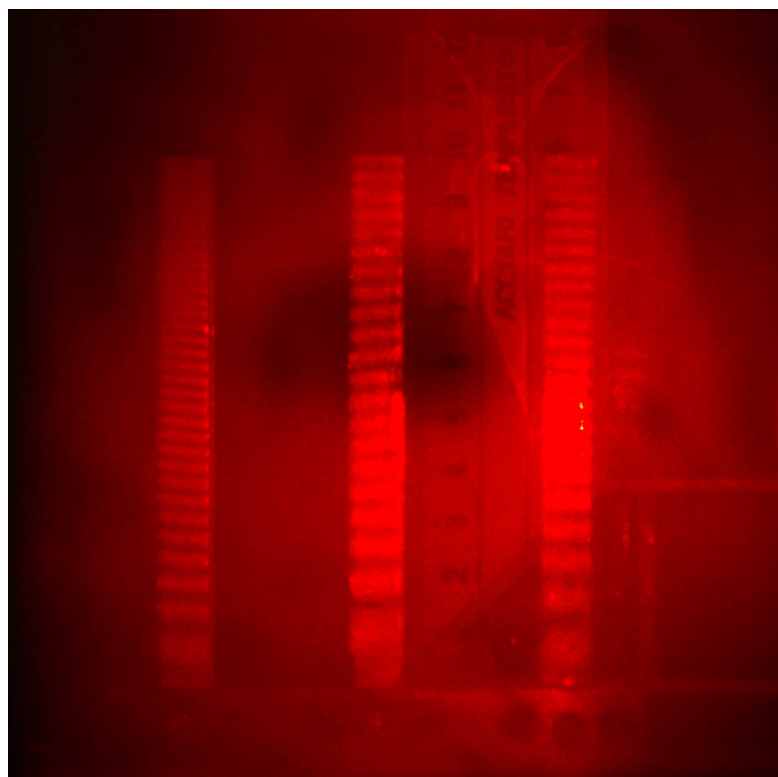


Figure 2.3: Interference pattern of the deflection of the beam (steel: left, brass: middle, aluminium: right)

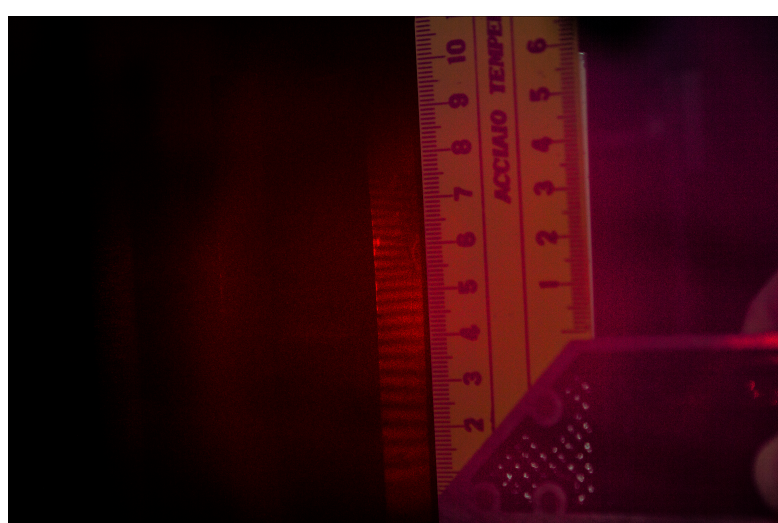


Figure 2.4: Measurement of the position of the minima using Photoshop

2.1.3 Real-time holography of oscillating Aluminium plate

The set-up was nearly identical to the one used double-holography. This time the object was a fixed round aluminium plate and the recording medium was a glass plate in a flooding system. A hologram of the stationary plate was recorded with following time intervals:

Exposure time : 1 min

Development time = 5 min

After the development process the resonant frequencies were determined. This was accomplished by exciting the plate with the mono-frequency sound of a speaker placed behind the plate. The hologram was illuminated by the reference beam and the oscillating plate by the object beam. Looking through the hologram when the correct frequencies were chosen made the observation of characteristic patterns on the plate possible. The interference patterns were enhanced by using a stroboscopic lighting technique with the Pockels cell. A very short time window to illuminate the plate was chosen with the Pockels cell. The signals of the acoustic frequency generator and the pulse generator of the Pockels cell were set to coincide at the maxima of the acoustic signal. The two signals were visualised on an oscilloscope (see Fig. 2.5).

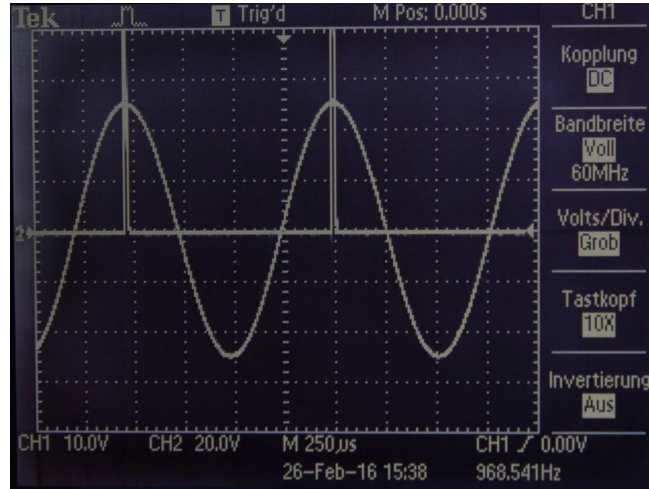


Figure 2.5: Signal setting for the stroboscopic lighting

The quality of the image was perfected by varying volume and frequency of the sound as well as the pulse duration and delay of the Pockels cell.

2.1.4 Fourier interferometry

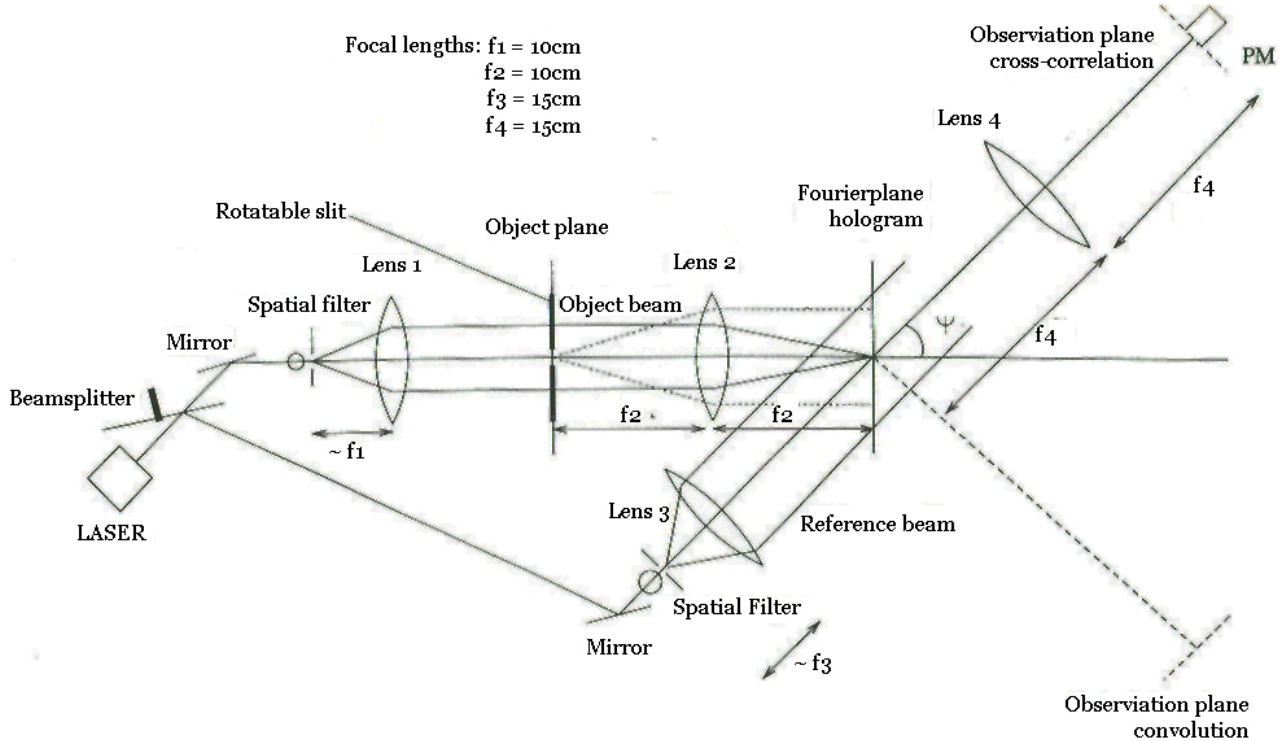


Figure 2.6: Experimental set-up for the cross-correlation measurement

In the last part of the experiment the previous set-up was altered (see Fig. 2.6). Collimator lenses were placed behind the spatial filters (roughly at focal length). The reference beam remained unchanged. A 2f-system with a vertical slit (width $50\text{ }\mu\text{m}$ and length 9 mm) was placed in the object beam. The recording medium (glass plate in the flooding system) was positioned exactly in the Fourier plane of the 2f-system. Then a hologram of the Fourier transformed slit (diffraction pattern) was recorded. The exposure time was increased (overexposing the photo plate) in order to make the higher order maxima more visible.

Exposure time : 2 min

Development time = 5 min

Thereupon a lens was positioned at focal length in direction of the reference beam , which was then blocked. This effectively created a 4f-system with the hologram acting as a multiplicative transmission mask and the autocorrelation in the focal plane of the second lens. The cross-correlation was created by rotating the slit and could be studied by taking photographs with a camera. A neutral-density filter and a polarising filter were used to maximise the image quality. The angle between the slits was roughly estimated as there was no other way to measure it. An attempt was made to analyse the real image of the convolution on a screen in a 90° angle to the cross-correlation. The quality of this image was greatly inferior and the effect was not observed.

3 Evaluation

3.1 Michelson Interferometer

Following interference pattern was visible on the screen (Fig. 3.1):

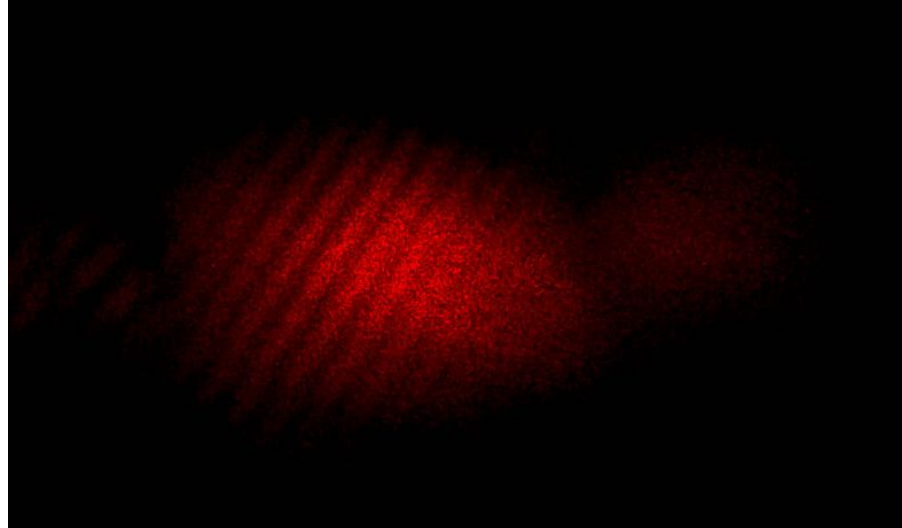


Figure 3.1: Observed interference pattern with the Michelson interferometer

The picture was taken with the interferometer arm lengths:

$$L_1 = (7.5 \pm 0.5) \text{ cm} \quad L_2 = (43 \pm 0.3) \text{ cm} \quad \Rightarrow \quad \Delta L = 35.5 \text{ cm}$$

When mirror 2 was moved right to the edge of the optical table the interference pattern was still visible. Further increasing L_2 to 181.8 cm (by placing the mirror on a neighbouring table) led to the dissolving of the stripy interference pattern. However it is safe to say that the coherence length of the laser light by far exceeded the value of 30 cm stated in [2]. Therefore the coherence was sufficient and holography was possible.

The interference pattern proved to be rather susceptible to outer influence. Talking, walking and blowing air into one of the interferometer arms shook the pattern but did not entirely destroy it. Further increasing the optical path difference with the loud sound of the speakers or holding a lighter into one of the interferometers arms destroyed the pattern completely. These findings were kept in mind while performing the subsequent holographic measurements with extreme diligence.

3.2 Determination of the elastic moduli of the beam materials

Only two of the recorded holograms produced clear interference patterns. Choosing a lighter weight for aluminium and a heavier weight for steel resulted in more evaluable patterns as these materials have the highest/lowest elastic modulus. The measurements were performed with the same weights but different angles of the beams and a slight alteration in the light intensities.

The geometry of the beam deflection can be viewed in Fig. 3.2. The optical path difference ($\Delta\phi$) created caused by the deflection (y) is given by:

$$\Delta\phi = \frac{2\pi}{\lambda} \cdot y \cdot (\cos(\alpha) + \cos(\beta)) \quad (16)$$

Minima occur with following phase difference:

$$\Delta\phi = (2n + 1) \frac{\pi}{2} \quad n = 0, 1, 2, \dots \quad (17)$$

Hence the deflection of the beam at the position of the minima is given by:

$$y = \frac{\lambda}{4} \cdot (2n + 1) \cdot \frac{1}{\cos(\alpha) + \cos(\beta)} \quad (18)$$

The angles α and β were measured with a set square with an uncertainty $s_\alpha = s_\beta = 3^\circ$. The uncertainty for the deflection can then be calculated with error propagation:

$$s_y = \frac{y}{(\cos(\alpha) + \cos(\beta))} \sqrt{(\sin(\alpha)s_\alpha)^2 + (\sin(\beta)s_\beta)^2} \quad (19)$$

The uncertainty of the deflection is strikingly small (as can be seen from the fits on the later pages).

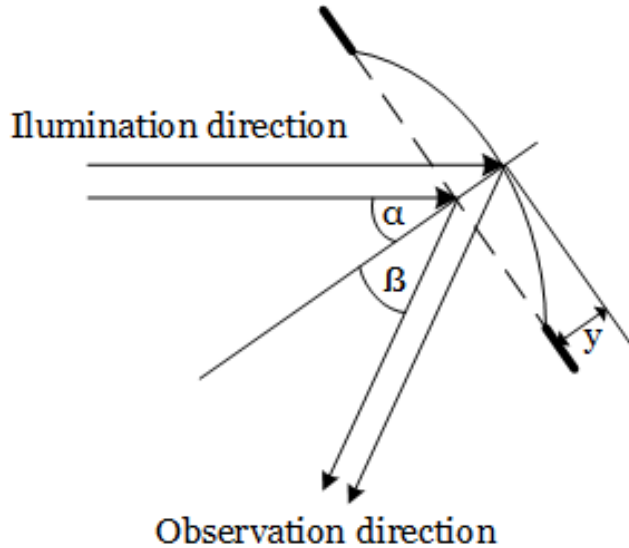


Figure 3.2: Geometry of the deflected metal beam

A cubic function was fitted to the experimentally determined data (derivation in section 5.1):

$$y = P_1 \left(0.0495x^2 - \frac{x^3}{6} \right) + P_2x + P_3 \quad (20)$$

Here y is the deflection, x is the distance from clamping point to minimum and P_{1-3} are fit parameters. P_2 and P_3 were introduced in order to compensate the tilting of the beams. The elastic modulus (E) can be extracted from fit parameter P_1 with this formula:

$$E = \frac{12F_g}{P_1bc^3} = \frac{12mg}{P_1bc^3} \quad (21)$$

The other parameters in the formula are:

$$\text{Mass of weight : } m$$

$$\text{Acceleration of gravity : } g = 9.81 \frac{\text{m}}{\text{s}^2}$$

$$\text{Width of the beam : } b = (10.5 \pm 0.02) \text{ mm}$$

$$\text{Thickness of the beam : } c = (5.05 \pm 0.02) \text{ mm}$$

The width and the thickness of the beam were measured with a calliper and the uncertainty represents the reading accuracy. In light of the far greater relative error of the fit parameter P_1 (see below), these errors (relative error $\approx 0.4\%$) were negligible. The mass of the weights was given and treated as free from error.

The results of the fits are listed in table (1) and the fits can be seen in Fig. (3.3-3.8).

Material	m/g	$\alpha/^\circ$	$\beta/^\circ$	P1	s_{P_1}	χ^2_{red}	E/GPa	s_E/GPa
Aluminium	10	42	8	0.008	0.001	0.4069	109	13
Aluminium	10	36	4	0.0100	0.0013	0.3421	87	12
Brass	20	36	4	0.017	0.004	2.0710	100	26
Brass	20	36	4	0.0150	0.0008	0.6201	116	7
Steel	50	42	8	0.0207	0.0015	0.8785	211	16
Steel	50	36	4	0.017	0.003	11.23	255	38

Table 1: Experimental data for the elastic moduli

In principle all of the fits seem to represent the data fairly well. The χ^2 value of the fits in Fig. (3.3, 3.4, 3.6 and 3.7) are smaller than one, which is explainable by the data being slightly 'overfitted'. This is most likely due to incorrect estimation of the uncertainties. In contrast the χ^2 values of the fits in Fig. (3.5+3.8) are too large. The corresponding interference patterns had the worst quality of the ones which were evaluated. This manifests itself in the scattering of the measurement points. The uncertainty for the elastic modulus s_E was calculated by using error propagation:

$$s_E = E \frac{s_{P_1}}{P_1} \quad (22)$$

The only contributing error was s_{P_1} which was extracted directly from the fits. A weighted mean of the values was calculated for the final values of E . The formula for the weighted mean and its uncertainty are:

$$\bar{E} = \frac{\sum_i \frac{E_i}{s_i^2}}{\sum_i \frac{1}{s_i^2}} \quad s_{\bar{E}} = \frac{1}{\sqrt{\sum_i \frac{1}{s_i^2}}} \quad (23)$$

The final values and literature values are:

Material	E_{Exp} / GPa	E_{Lit} / GPa
Aluminium	97 ± 9	72
Brass	115 ± 7	100
Steel	217 ± 15	195

Table 2: Literature and experimental values for the elastic moduli

The experimental values for steel has the largest uncertainty and is compatible with the literature value in a range of 2σ . The experimental values for aluminium and brass are compatible in a 3σ range. The reasons for this discrepancy are discussed in section 4.2.

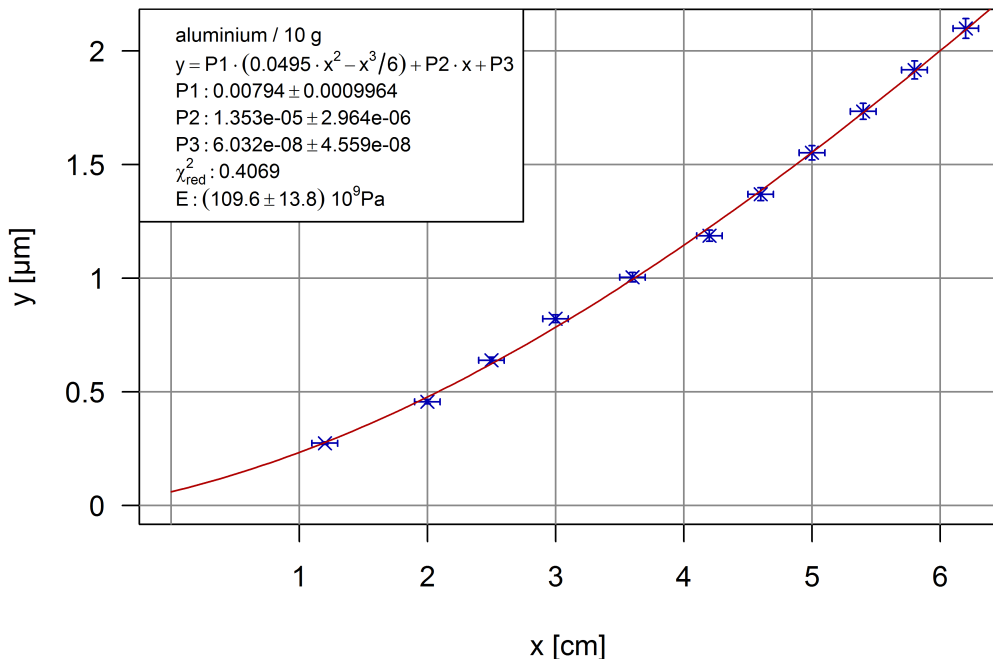


Figure 3.3: Aluminium, measurement 1: 10g weight

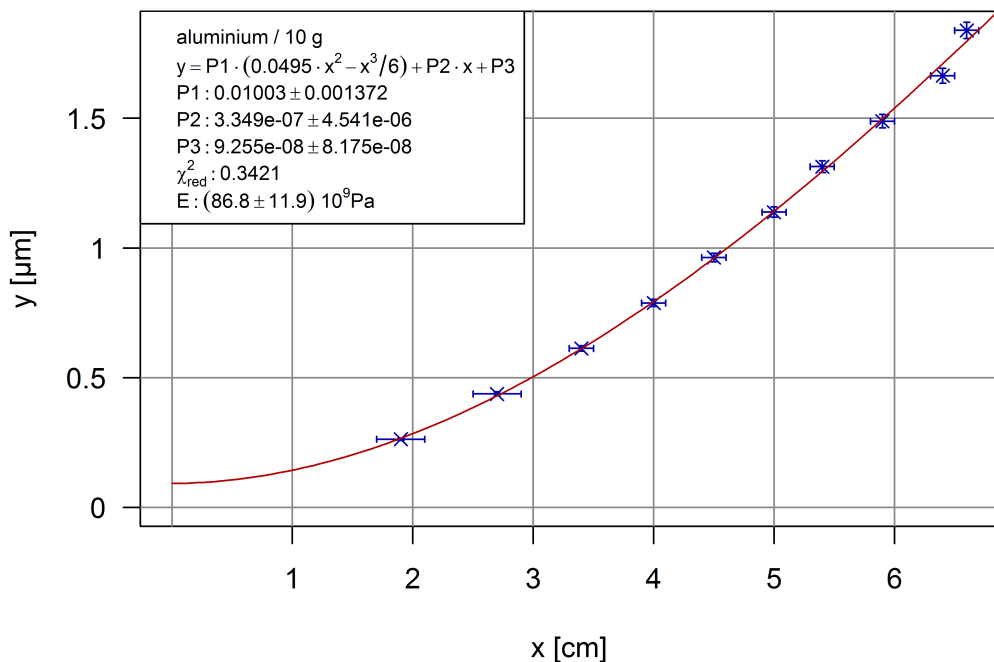


Figure 3.4: Aluminium, measurement 2: 10g weight

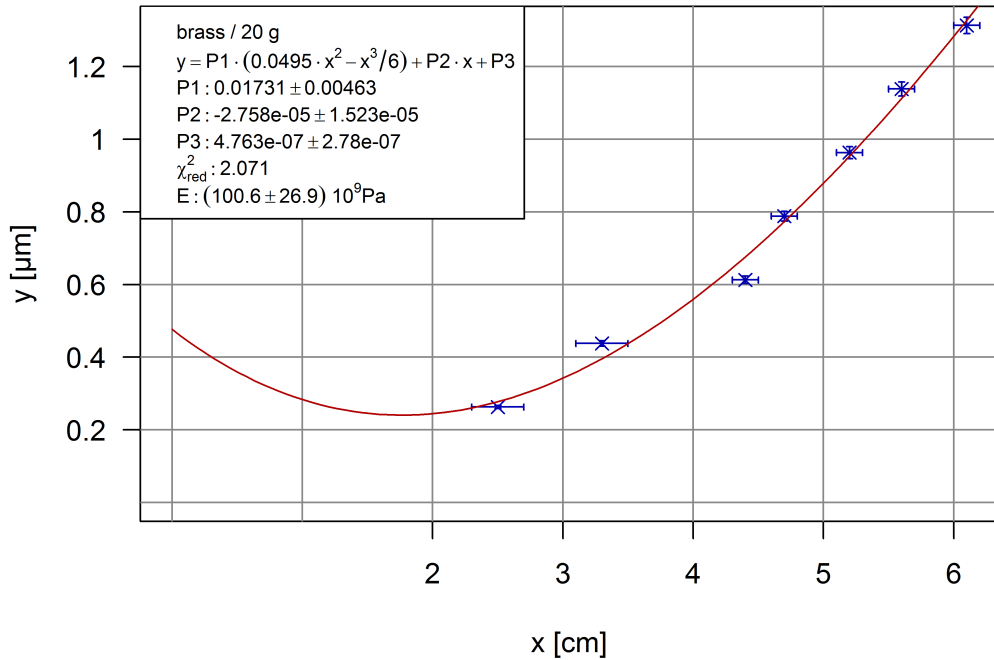


Figure 3.5: Brass, measurement 1: 20g weight

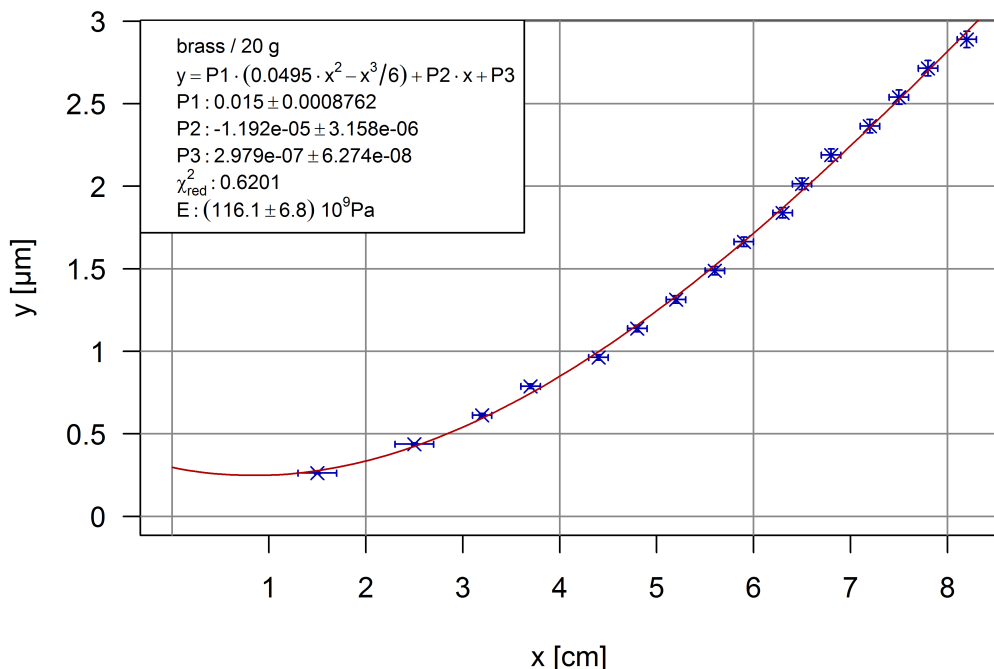


Figure 3.6: Brass, measurement 2: 20g weight

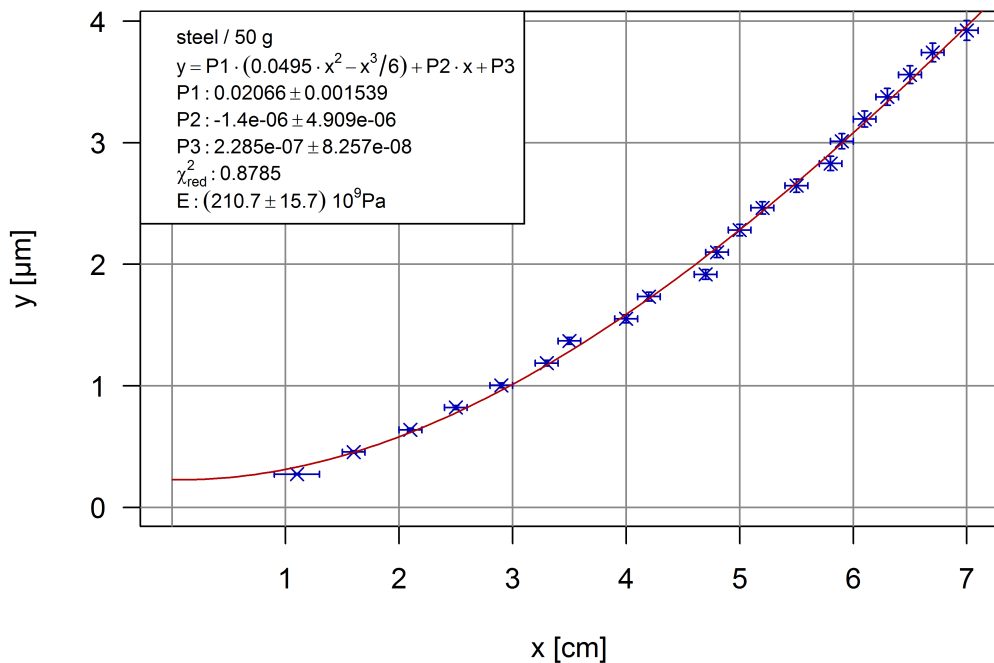


Figure 3.7: Steel, measurement 1: 50g weight

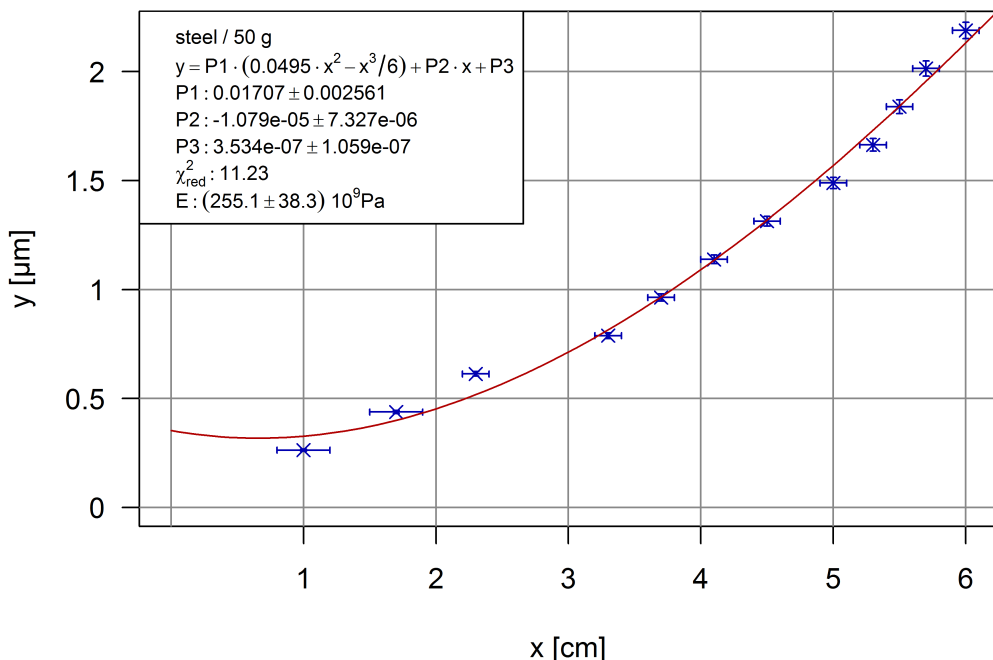


Figure 3.8: Steel, measurement 2: 50g weight

3.3 Measurement of the resonant frequencies of the aluminium plate

Six resonant frequencies were observed using the real-time holography technique. The photographs of the interference pattern can be seen in Fig. (3.9-3.14) below. To increase the visibility of the pattern the colour has been removed and the contrast and brightness adjusted. The theoretical predictions for the shapes of the different modes can be seen in section 5.2 (Fig. 5.3).

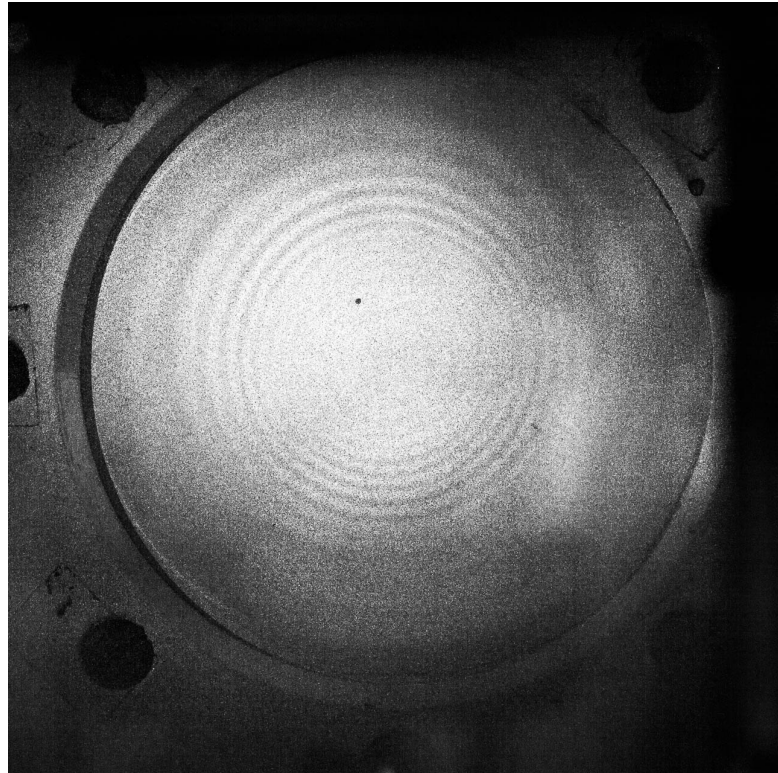


Figure 3.9: f_{00} mode of the plate (442 Hz)

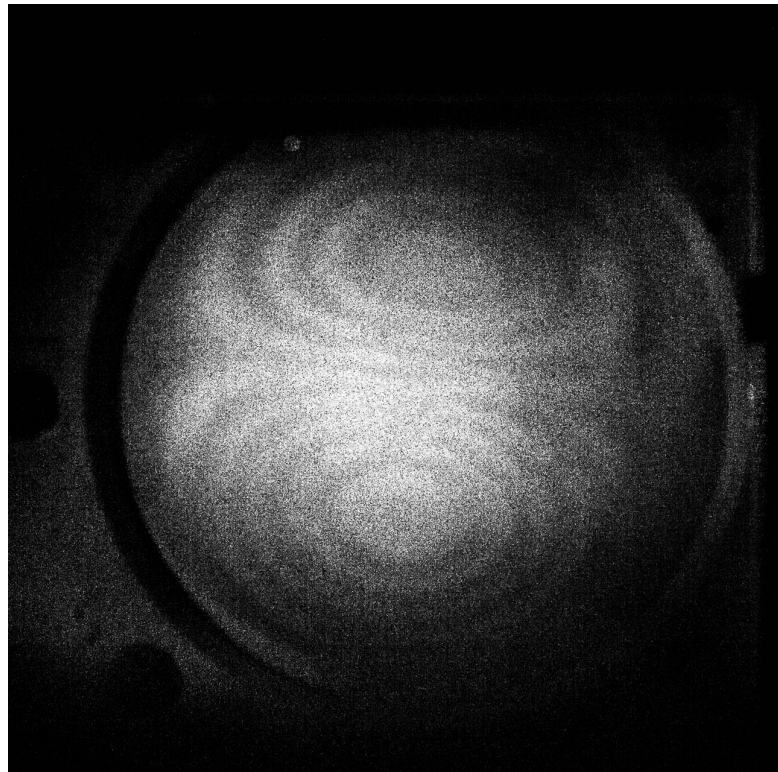


Figure 3.10: f_{10} mode of the plate (1068 Hz)

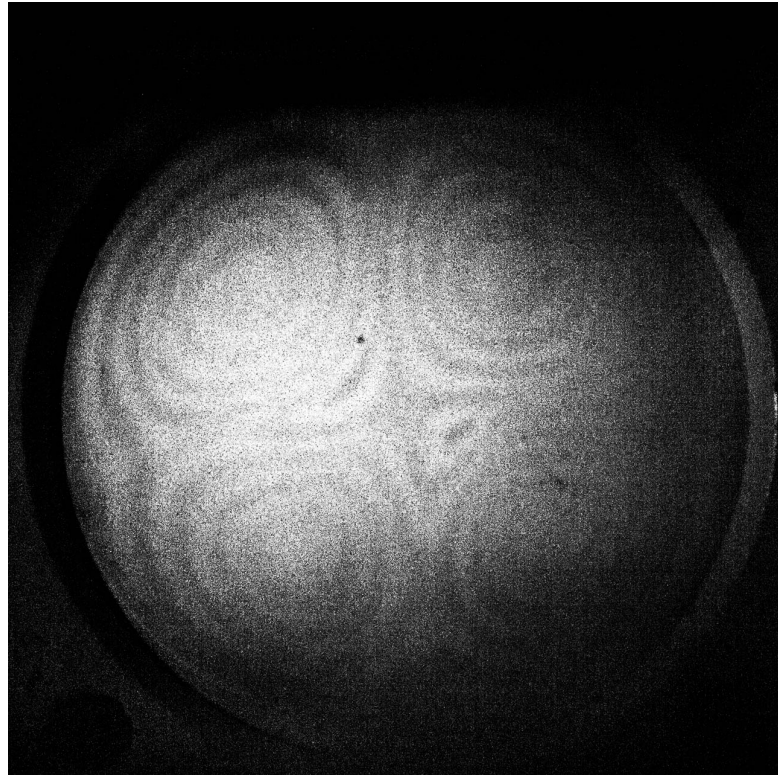


Figure 3.11: f_{20} mode of the plate (1738 Hz)

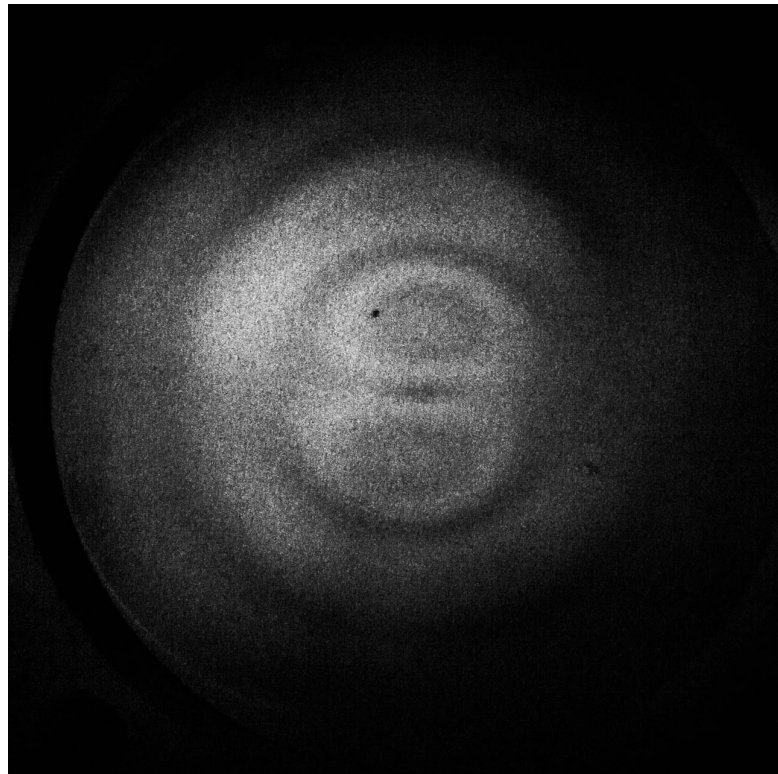


Figure 3.12: f_{11} mode of the plate (2931 Hz)

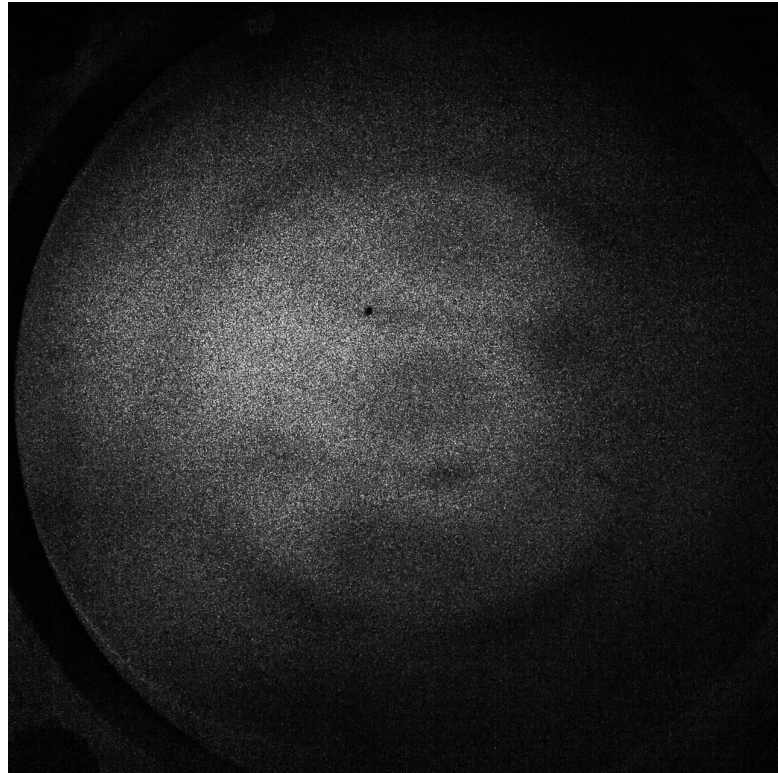


Figure 3.13: f_{21} mode of the plate (4129 Hz)

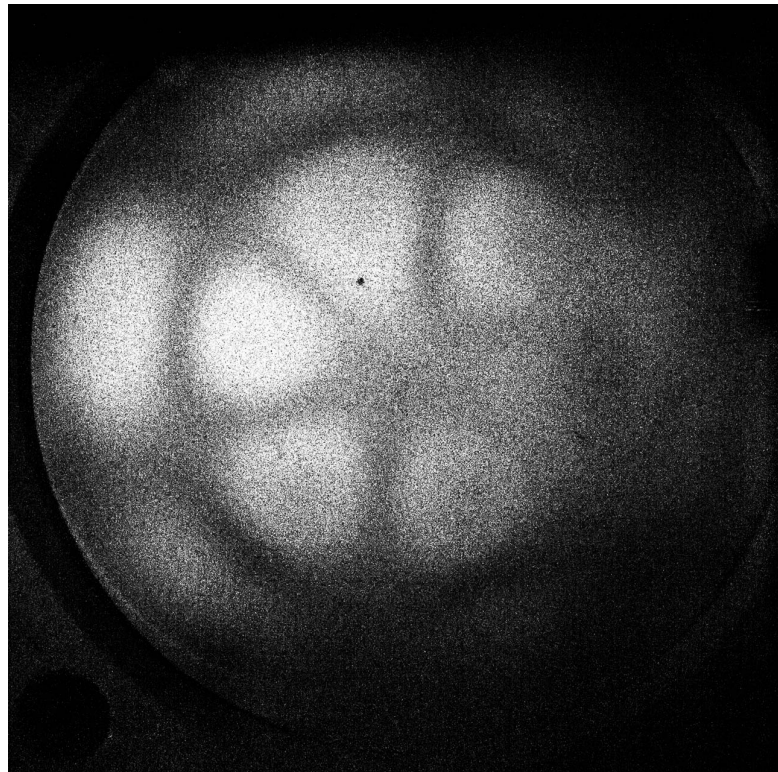


Figure 3.14: f_{31} mode of the plate (5429 Hz)

The high quality photographs convey the clarity with which the modes were able to be observed. Solely the f_{21} mode (Fig. 3.13) could not be captured in as high quality as the other modes. The measured resonant frequencies and their uncertainties are listed in table 3. In principle fine tuning was only possible at the lower frequencies, because the precise setting of the frequency in a range of 10 000 Hz was impossible. However this was compensated by the fact that the higher resonant frequencies were far sharper and therefore easier to find. This was considered in the estimation of the uncertainties. The theoretical calculation of the resonant frequency led to unrealistically high results (see calculation in section 5.2), which were ten times as high as the experimental values. For this reason a comparison with these values was deemed to be not meaningful. Instead of this the measured values were compared with literature values of unknown origin. These can also be found in table 3.

mode	f_{exp}/Hz	$s_{f_{exp}}/\text{Hz}$	f_{lit}/Hz
f_{00}	442	15	448
f_{10}	1068	10	983
f_{20}	1738	10	1592
f_{11}	2931	10	2854
f_{21}	4149	20	4090
f_{31}	5429	10	-

Table 3: Literature and experimental values for the resonant frequencies

With the exception of the first resonant frequencies, the values are incompatible (discrepancy of 59-146 Hz). The measured frequencies are generally higher than the literature values, but not by a constant factor. With regard to the dubious nature of these literature values the validity of the experimental values is not diminished.

To substantiate the claim that the measured values are satisfactory, the experimental frequencies were plotted against the theoretical values of x_{mv}^2 (see calculation in 5.2). The theoretical model suggests that there should be a linear dependence between these values. The resulting plot and linear fit can be viewed in Fig. (3.15).

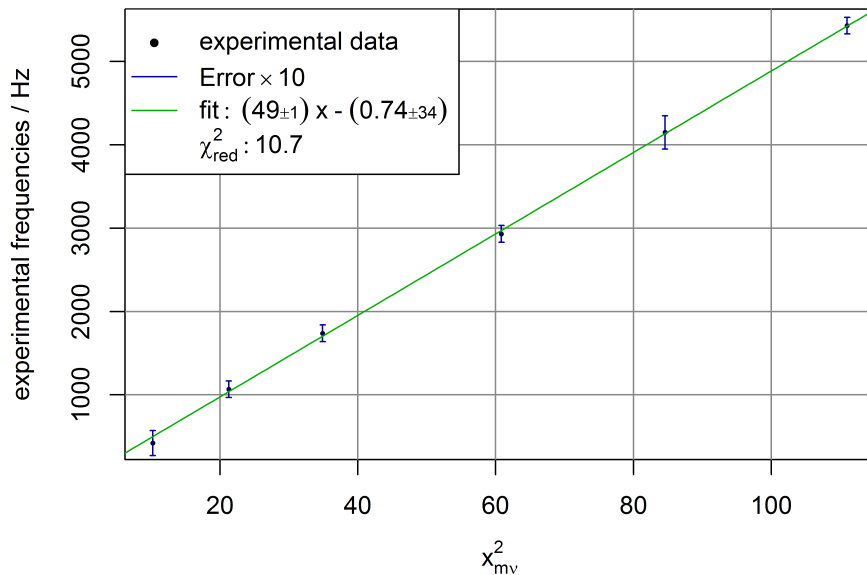


Figure 3.15: Plot of experimental values and x_{mv}^2 with a linear fit (error bars stretched by factor 10)

A linear relationship between the values exists. The estimated uncertainties were most possibly too small as the frequency generator and counter were of low quality. Because there is a linear relationship, the theoretical model describes the situation correctly (in principal). The source of error is most probably to be found in the material constants involved in the theoretical formula (see section 33) and the idealisation of a completely round plate.

3.4 Cross-correlation of two slits

The following pictures of the cross-correlation were recorded (angles between the slits were roughly estimated):

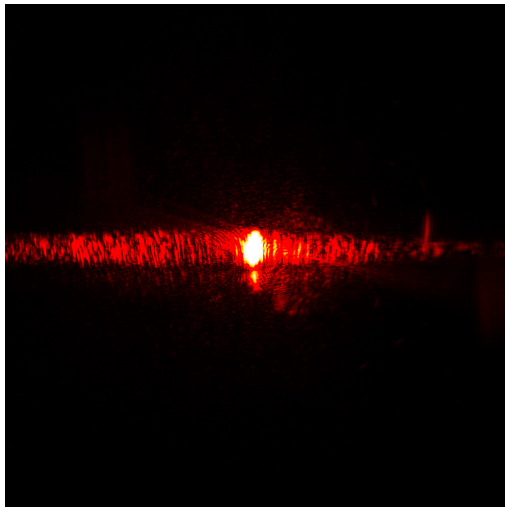


Figure 3.16: Autocorrelation of a slit



Figure 3.17: Cross correlation 10°

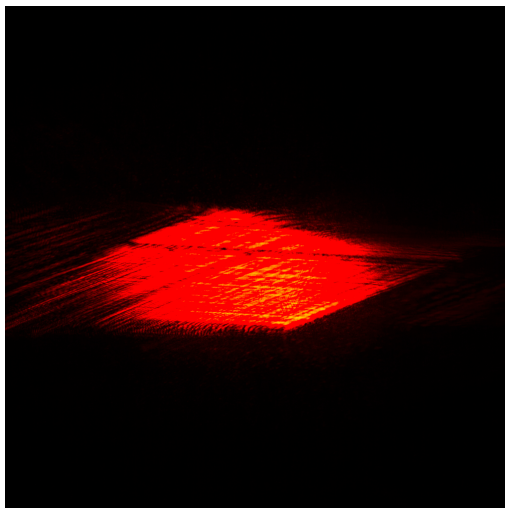


Figure 3.18: Cross correlation 20°

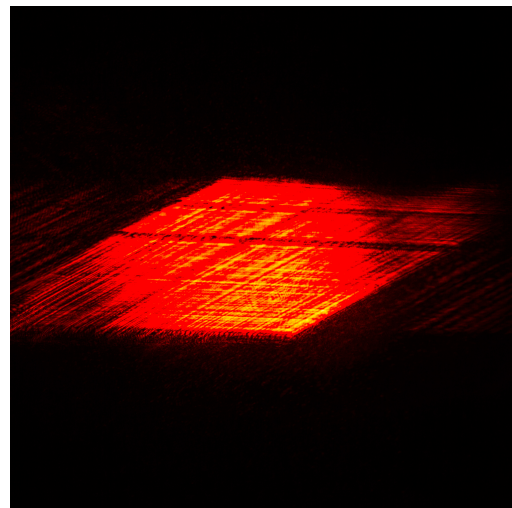


Figure 3.19: Cross correlation 30°

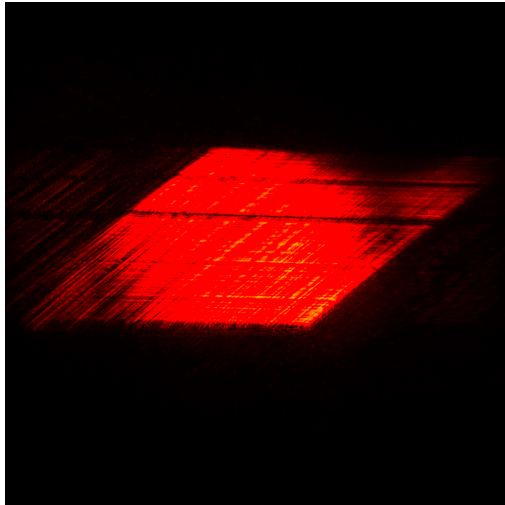


Figure 3.20: Cross correlation 45°

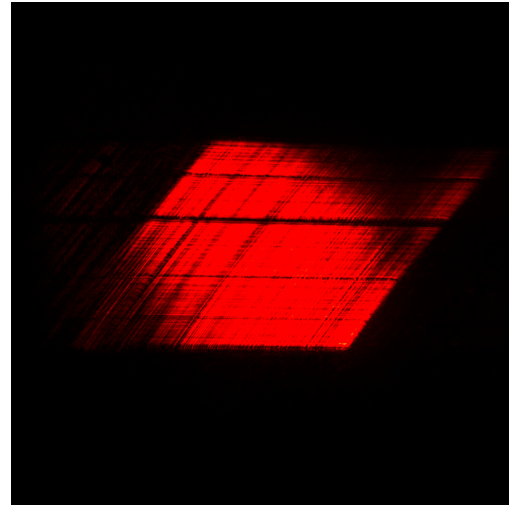


Figure 3.21: Cross correlation 60°

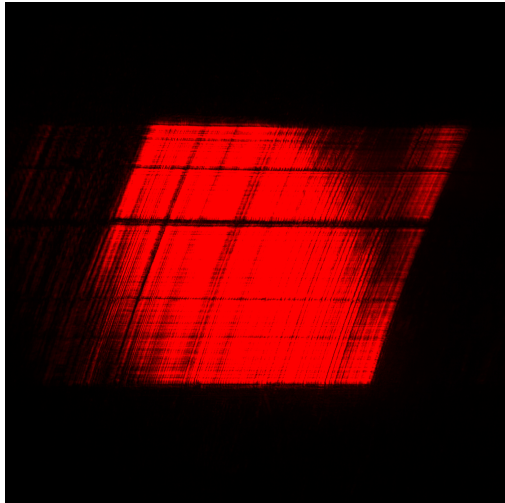


Figure 3.22: Cross correlation 80°

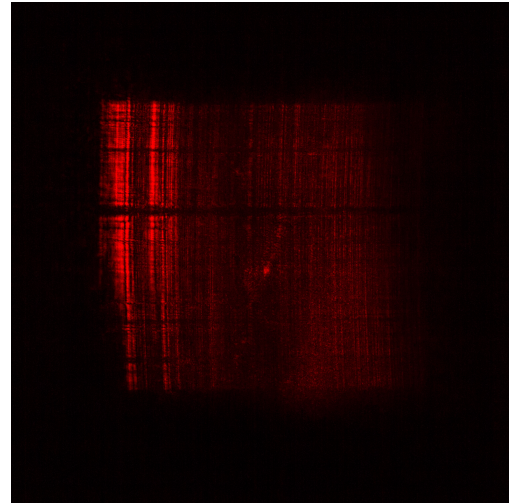


Figure 3.23: Cross correlation 90°

These pictures were compared with the simulated cross-correlations given in [1] (Fig. 3.24). The experimental results match the theoretical prediction well. As this part of the experiment was of qualitative nature, an uncertainty for the angle of the slits is of little use.

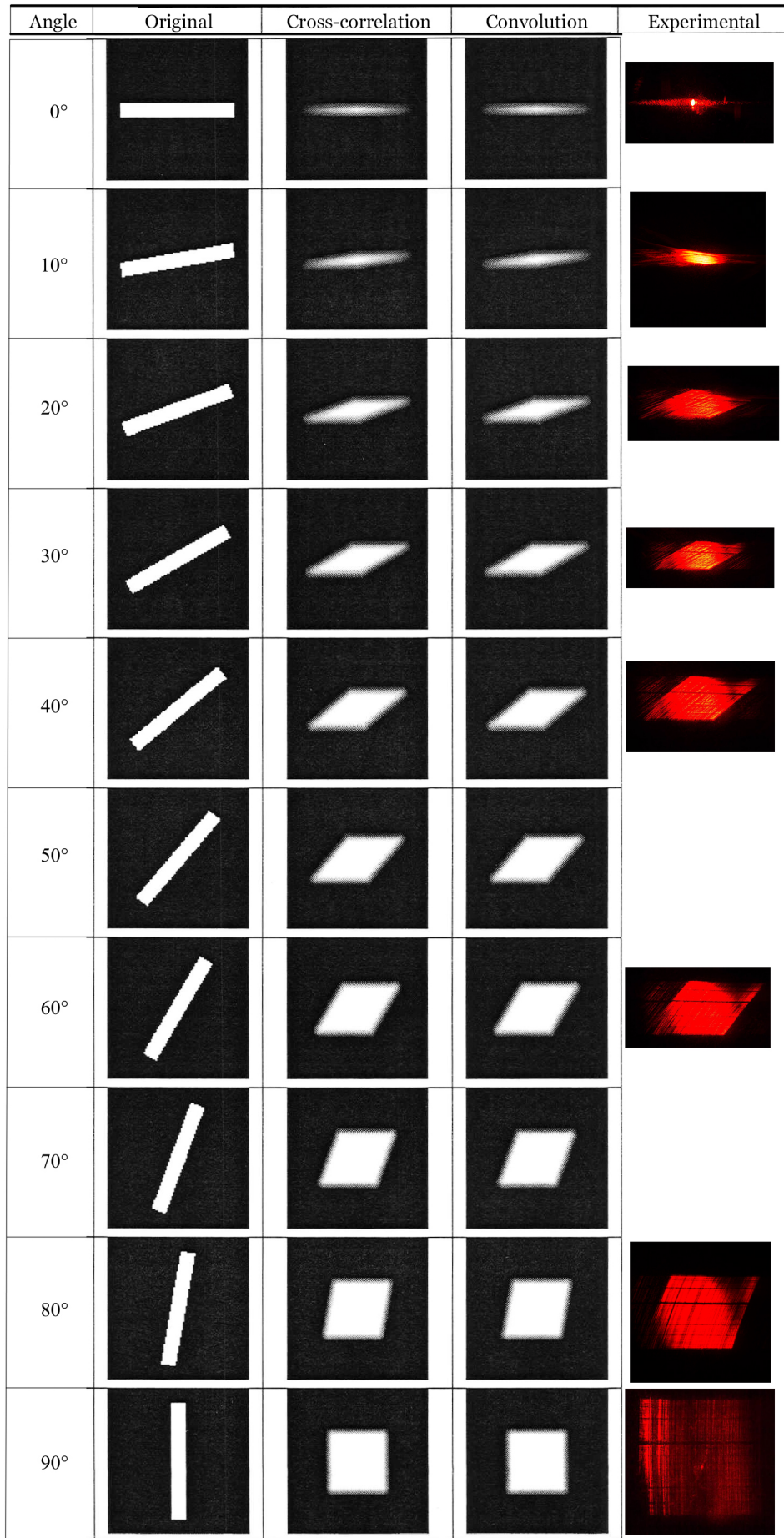


Figure 3.24: Comparison of experimental and simulated cross-correlation (original from [1])

4 Summary

4.1 Michelson Interferometer

With the help of the Michelson interferometer sufficient coherence of the laser light was verified. The coherence length of the laser was far longer than the optical bench. Furthermore the susceptibility of the interferometric set-up to external disturbances was established.

4.2 Determination of the elastic moduli of the beam materials

The elastic moduli of the aluminium, brass, and steel beam were determined with the double-exposure holographic interferometry technique. The results are listed in table 4.

Material	E_{Exp} / GPa	E_{Lit} / GPa
Aluminium	97 ± 9	72
Brass	115 ± 7	100
Steel	217 ± 15	195

Table 4: Summary of experimental and literature values for the elastic moduli

All the values are compatible with their corresponding literature values in a range of 3σ , which is acceptable. The sole source for the stated uncertainty were the uncertainties given by the fit routine. The meaningfulness of these uncertainties can therefore be called into question.

A number of factors may have had an effect on the outcome of the measurements. The experimental elastic moduli are all too high. A high elastic modulus indicates a high stiffness of the material. This means that the position of the beams did not change as much as anticipated and implies that there may have been a systematic error. The most obvious explanation are impurities in the material of the examined beams. Considering the age of the beams one can assume that the beams (especially aluminium with the lowest elastic modulus) may have been permanently altered by fatigue and therefore were not bent as much.

A further problem was caused by the photographic film, which had visible patterns on them before exposure to light. The pattern was still visible on the developed holograms and was a considerable hindrance in the measurement of the minima position.

Another complication was the observed distortion of the final interference pattern. This led to "bending" interference lines obscuring the exact position of the minima. This was made worse by the noticeable dependence on the observation direction, which was most likely not correctly considered by the formula used for the calculation of the deflection.

Finally it has to be mentioned that the intensity of the object beam greatly varied for the individual beam. Brass was the only beam to be fully engulfed in light with a constant intensity. The aluminium beam to the right was exposed to the lowest intensity of the three. Recording a double-exposure hologram of the beams separately would increase the quality of the results.

4.3 Measurement of the resonant frequencies of the aluminium plate

The measured resonant frequencies of the round plate were:

mode	f / Hz
f_{00}	(422 ± 15)
f_{10}	(1068 ± 10)
f_{20}	(1738 ± 10)
f_{11}	(2931 ± 10)
f_{21}	(4149 ± 20)
f_{31}	(5429 ± 10)

Table 5: Experimentally obtained resonant frequencies of the aluminium plate

The proportionality of these values to x_{mn}^2 , which is theoretically predicted could be shown. As the calculation of the theoretical frequencies failed to produce plausible results, a comparison with literature values of unknown origin was carried out. The measured resonant frequencies were (with the exception of the first mode) higher than the literature values. The lowest frequency was visible at a very broad frequency range and most likely was also higher. The main reason for the discrepancy are most likely abnormalities in the aluminium alloy, which were not reflected in the material constants involved in the calculation of the literature values.

Apart from this it is highly unlikely that the fixed plate behaved precisely as the idealisations implied by the theoretical mode suggest. The plate was held in place by eight screws on a rectangular holder which was also excited by the sound waves. This may have also altered the resonant frequencies as the strength with which the sides were fixed may have differed.

A further source of error was the frequency generator with which it was impossible to set the frequency accurately at high values. This was accompanied by the fact that fluctuations of the frequency displayed by the counter occurred at high frequencies. Both to the detriment of the precision required by measurements with holographic interferometry.

4.4 Cross-correlation of two slits

The expected patterns for the cross-correlation could be observed in high quality and reproduced the simulated data. As the measurement was merely of qualitative nature, the results were very good. The main difficulty was the correct positioning of the components (Fourier transforming lenses, slit and holographic plate). Even slight deviations of the required distances led to a shift of the diffraction pattern, rendering the hologram useless. A further problem was that in order to see the cross-correlation one had to look into the collimated laser beam, which is a serious health and safety hazard. Luckily this could be avoided by using a camera to examine the pattern. Alternatively the real image of the convolution could be analysed. However the effect was barely noticeable on the screen. Furthermore a narrower slit would have led to the appearance of higher order diffraction maxima, which may have further increased the quality of the correlation. However the resolution imposed by the recording medium is insufficiently high and the diffraction pattern would not be correctly recorded.

5 Appendix

5.1 Calculation for the deflection of a beam

A sketch of the deflected beam containing all the relevant variables can be seen in Fig.(5.1):

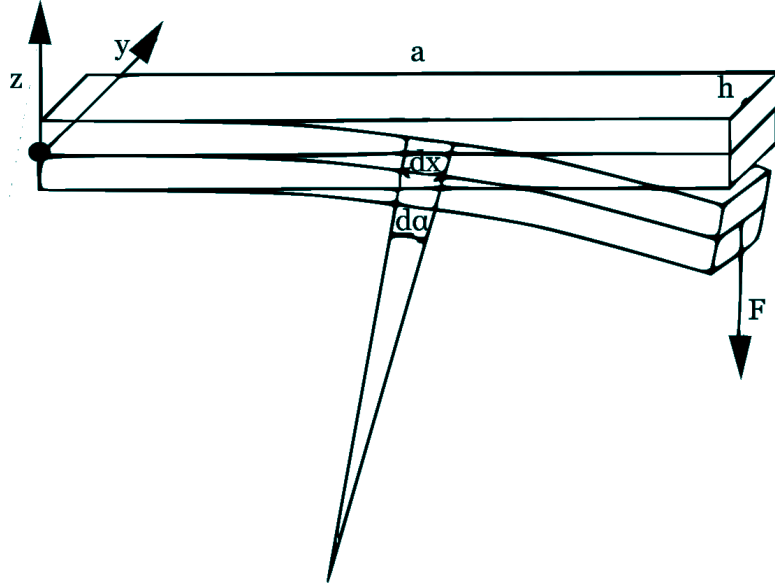


Figure 5.1: Geometry of the beam deflection

The relative change in length $\frac{\Delta l}{l}$ caused by a force dF acting on a cross-section element $dz dy$ is given by (E is the elastic modulus):

$$\frac{\Delta l}{l} = \frac{1}{E} \frac{dF}{dz dy} \quad (24)$$

So the force is:

$$dF = \frac{Ez}{r} dz dy \quad (25)$$

The force causes a torque T :

$$T = \int z dF = \frac{E}{r} \int z^2 dz dy \quad (26)$$

For a rectangular cross-section this becomes:

$$T = \frac{E}{r} \int_{y=0}^b \int_{z=-\frac{c}{2}}^{\frac{c}{2}} z^2 dz dy = \frac{Ebc^3}{12r} \quad (27)$$

If the beam is in equilibrium this torque is compensated by the torque T' originating from the force acting at the end of the beam $x = a$. The absolute value of T' at the position x is:

$$T' = F(a - x) \quad (28)$$

The equilibrium condition is:

$$\frac{Ebc^3}{12r} = F(a - x) \quad (29)$$

As the deflection of the beam is small, the curvature is approximated by $\frac{1}{r} = -\frac{d^2x}{dx^2}$. The above equation becomes:

$$\frac{d^2z}{dx^2} = -\frac{12F}{Ebc^3}(a - x) \quad (30)$$

Integrating twice and making use of the fact that z and $\frac{dz}{dx}$ disappear at $x = 0$ leads to the final solution:

$$z = -\frac{12F}{Ebc^3} \left(\frac{ax^3}{2} - \frac{x^3}{6} \right) \quad (31)$$

The length of the beam (a) was measured and found to be 9.9 cm. Inserting this value into equation (31) and absorbing values in the fit parameter P_1 leads to the fit formula. P_2 and P_3 are introduced to account for the tilting of the beam.

$$y = P_1 \left(0.0495x^2 - \frac{x^3}{6} \right) + P_2x + P_3 \quad (32)$$

5.2 Resonant frequency of a fixed round plate calculations

The formula for the calculation of the resonant frequencies is (from [2]):

$$f_{m\nu} = \frac{x_{m\nu}^2}{2\pi R^2} h \sqrt{\frac{E}{12\rho(1-\mu^2)}} \quad (33)$$

R is the radius and h the thickness of the plate. ρ is the density, E the elastic modulus and μ the Poisson's ratio of the material (in this case aluminium). The $x_{m\nu}$ values are the numerical solution to this equation (derivation on [2]):

$$J_m(ix)[J_{m-1}(x) - J_{m+1}(x)] - iJ_m(x)[J_{m-1}(ix) - J_{m+1}(ix)] = 0 \quad (34)$$

J being the *Bessel functions of the first kind* (see plot in Fig. 5.2), i the *imaginary unit* and m the number of the radial nodal line. This formula was solved with Mathematica (results in table 6). ν gives the number of circular nodal lines.

$x_{m\nu}$	$m = 0$	$m = 1$	$m = 2$	$m = 3$
$\nu = 0$	3.19622	4.61090	5.90568	7.14353
$\nu = 1$	6.30644	7.79927	9.19688	10.53670

Table 6: Calculated $x_{m\nu}$ values for the aluminium plate

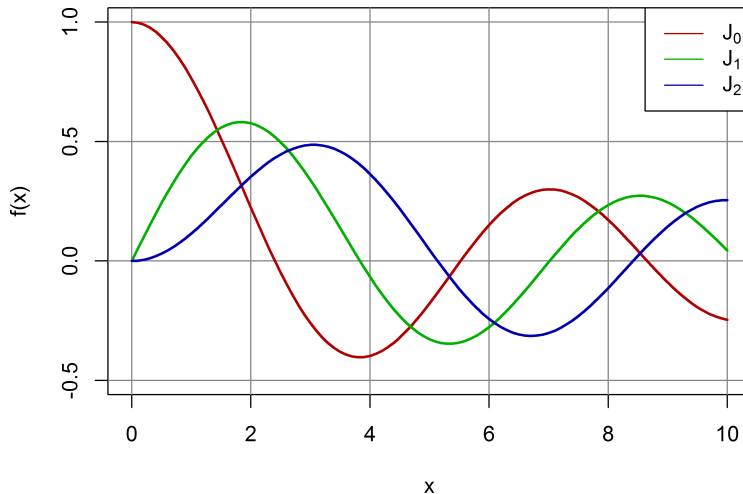


Figure 5.2: Bessel functions of the first kind (Order 0-2)

With the above values for $x_{m\nu}$ and following constants for the aluminium plate, the theoretical resonant frequencies were calculated (results in table 7):

$$R = (5.0 \pm 0.5) \text{ cm}$$

$$h = 5 \text{ mm}$$

$$E = 70 \text{ GPa}$$

$$\rho = 2700 \frac{\text{kg}}{\text{m}^3}$$

$$\mu = 0.34$$

$f_{m\nu}$	m = 0	m = 1	m = 2	m = 3
$\nu = 0$	5082	10577	17352	25388
$\nu = 1$	19787	30263	42081	55235

Table 7: Calculated resonant frequencies of the aluminium plate

These values are unrealistically high. An explanation for a discrepancy of this magnitude between the theoretical and experimental values can not be found. The measured resonant frequencies were:

mode	frequency / Hz
f_{00}	422
f_{10}	1068
f_{20}	1738
f_{11}	2931
f_{21}	4149
f_{31}	5429

Table 8: Experimentaly obtained resonant frequencies of the aluminium plate

The characteristic patterns pertaining to the different $x_{m\nu}$ values can be seen in Fig. (5.3) below:

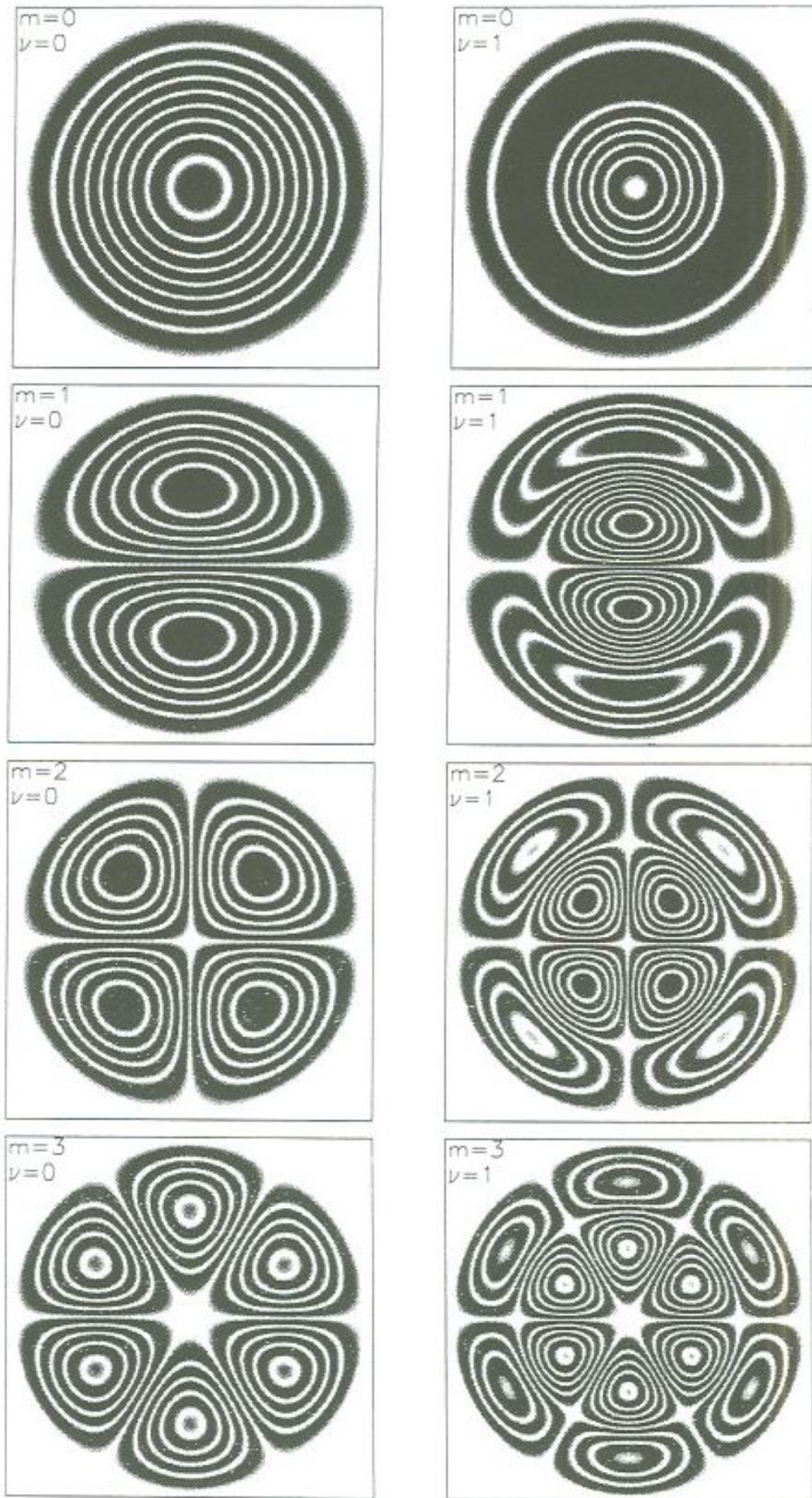


Figure 5.3: Oscillations of the plate at resonant frequencies for different values of $x_{m\nu}$ (from [2])

5.3 Measured data

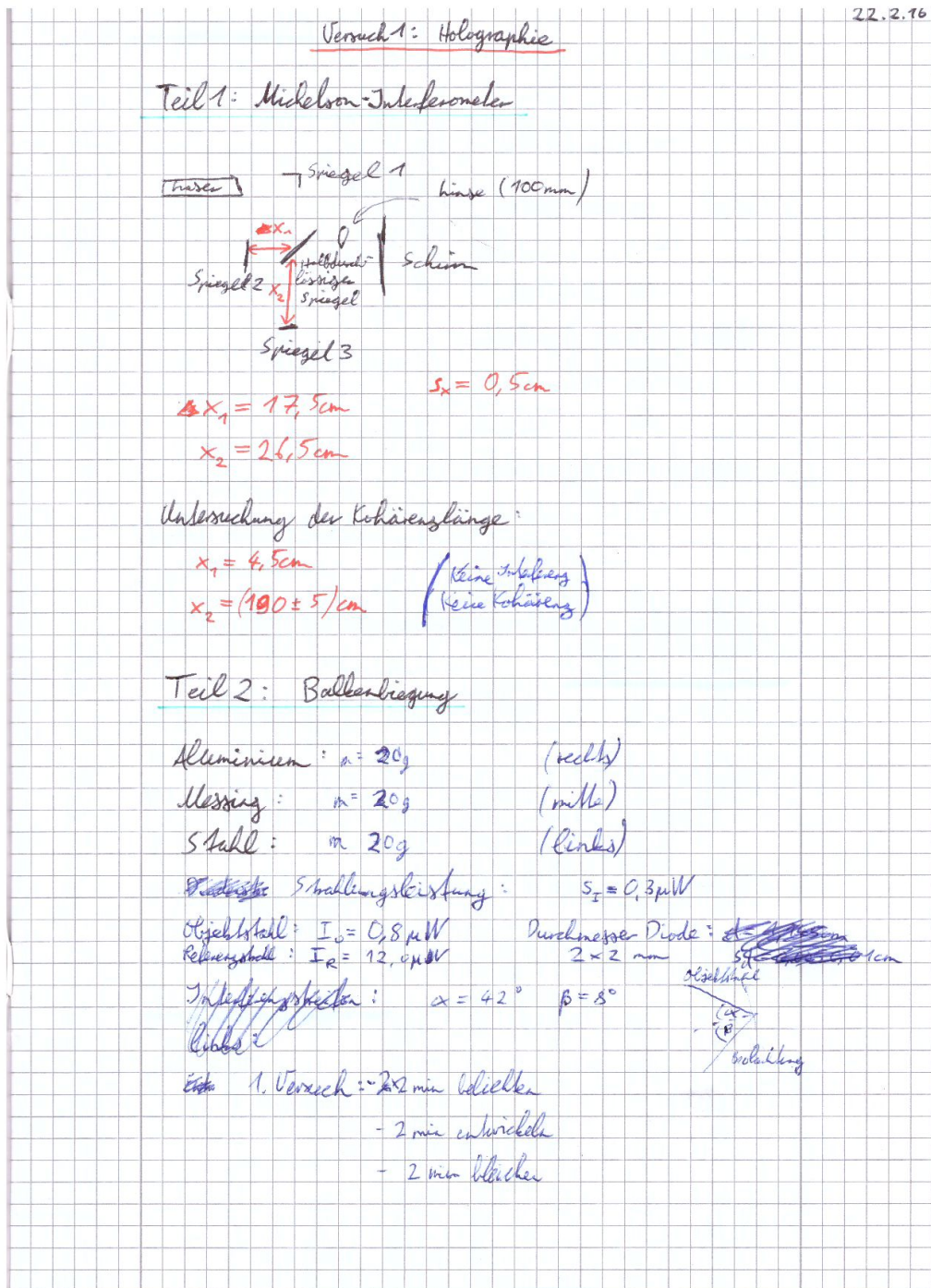


Figure 5.4: Laboratory journal entry page 1

2. Versuch:	- 2x 1 min belichten	23.2.16
	+ 1 min entwickeln	
	- 3 min blenden	
3. Versuch:	- 2x 3 min belichten	
	+ 1 min entwickeln	
	- 2 min blenden	
4. Versuch:	- 2x 70 s belichten	
	- 1 min entwickeln	
	- 2 2 min blenden	
5. Versuch:	- 2x 40 s belichten	1: 20; 20; 20
	- 1 min entwickeln	{ 1. Hologramm
	- 3 min blenden	Bleidittel relativ durchmischt
Positionen der Interferenzmaxima:		
<u>Stahl (links):</u> <u>uningespannt</u>		
Minimum	Position x / mm	5x/mm
1	15	2
2	27	1
3	36	1
4	43	1
5	52	1
6	58	1
7	65	1
8	71	1
9	77	1
10	83	1
11	89	1
12	95	1

Figure 5.5: Laboratory journal entry page 2

<u>Messing (links)</u>		
Minimeum	x/cm	s _x /cm
1	0,9	0,2
2	1,8	0,1
3	2,4	"
4	3,0	"
5	3,4	"
6	3,8	"
7	4,3	"
8	4,7	"
9	5,2	"
10	5,5	"
11	6,2	"
12	6,5	"
13	6,9	"
14	7,2	"
15	7,6	"
16	7,8	"
17	8,2	"
18	8,4	"
19	8,6	"
20	9,0	"

<u>Aluminium (rechts)</u>		
Minimeum	x/cm	s _x /cm
1,0	1,0	0,1
2	1,5	"
3	2,0	"
4	2,3	0,501

Figure 5.6: Laboratory journal entry page 3

Minimum	x/cm	s _x /cm
5	2,6	0,1
6	2,9	"
7	3,2	"
8	3,5	
9	3,9	
10	4,1	
11	4,4	
12	4,7	
13	4,9	
14	5,1	
15	5,5	
16	5,7	
17	5,9	

24.2.16

6. Versuch
Alles 20g

- 2x 1 min blicken
- 2 min entwölken
- lange blicken ...

~~Alles 20g (10g Messing) (10g Gold)~~
~~Messing (mitte) 70g~~
~~(links/rechts) 30g~~

⇒ Kein brauchbares Ergebnis

7. Versuch 3: 50; 20; 10
Stahl: 50g Messing: 20g Hl.: 10g

- 2x 40s blicken
- 2 min entwölken

Figure 5.7: Laboratory journal entry page 4

Minimum	x/cm	s _x /cm
1	1,1	0,2
2	1,6	0,1
3	2,1	"
4	2,5	"
5	2,9	"
6	3,3	"
7	3,5	
8	4,0	
9	4,2	
10	4,6	
11	4,8	
12	5,0	
13	5,2	
14	5,5	
15	5,8	
16	5,9	
17	6,1	
18	6,3	
19	6,5	
20	6,7	
21	7,0	

Very far back

Figure 5.8: Laboratory journal entry page 5

Messing Aluminium	x/cm	sx/cm
1	1,5	0,1
2	2,5	"
3	2,8	
4	3,5	
5	4,0	
6	4,4	
7	4,8	
8	5,3	
9	5,6	
10	6,0	
11	6,3	
12	6,9	
13	7,2	
14	7,6	
15	7,9	
Aluminium	x/cm	sx/cm
1	1,2	0,1
2	2,0	"
3	2,5	
4	3,0	
5	3,6	
6	4,2	
7	4,6	
8	5,0	
9	5,4	
10	5,8	

Figure 5.9: Laboratory journal entry page 6

	<u>Min.</u>	<u>x/cm</u>	<u>5x/cm</u>
	11	6,2	0,7
höhe der Ballen:	alle 80 (km)	je $(99,0 \pm 0,5)$ mm	
Dicke	" "	je $10,5 \text{ mm} \pm 0,02$	
Dicke	" "	$1,0 (5,05 \pm 0,02) \text{ mm}$	
$\alpha = (40 \pm 3)^\circ$		$\beta = (10 \pm 3)^\circ$	
Teil 3: Eigenschwingungen der Aluminiumplatte			
Pochels-Zelle Einstellungen:	DC-offset = 68		
		Pulse: 250	
eigenfrequenzen:	Hologramm 1 (Bildsch. erreichbar)		
Mode	f Hz	sf Hz	Foto
f_{00} 1	444	6	3429
f_{10} 2	1069	4	3441
f_{20} 3	1666	20	3481 3481
4	2815	30	3483
5	3911 / 3884	40	3472 / 3480
6	4201	50	3477
7			
Hologramm 2 (1min:5min)	gutes Bild		
Mode	f Hz	sf Hz	Foto
f_{00} 1	442	15	3445 / 3496 / 3508
f_{10} 2	1068	10	3445
f_{20} 3	1738		3566
f_{11} 4	2931	10	3581
f_{21} 5	4149	20	3582
f_{31} 6	5429	10	3593

Figure 5.10: Laboratory journal entry page 7

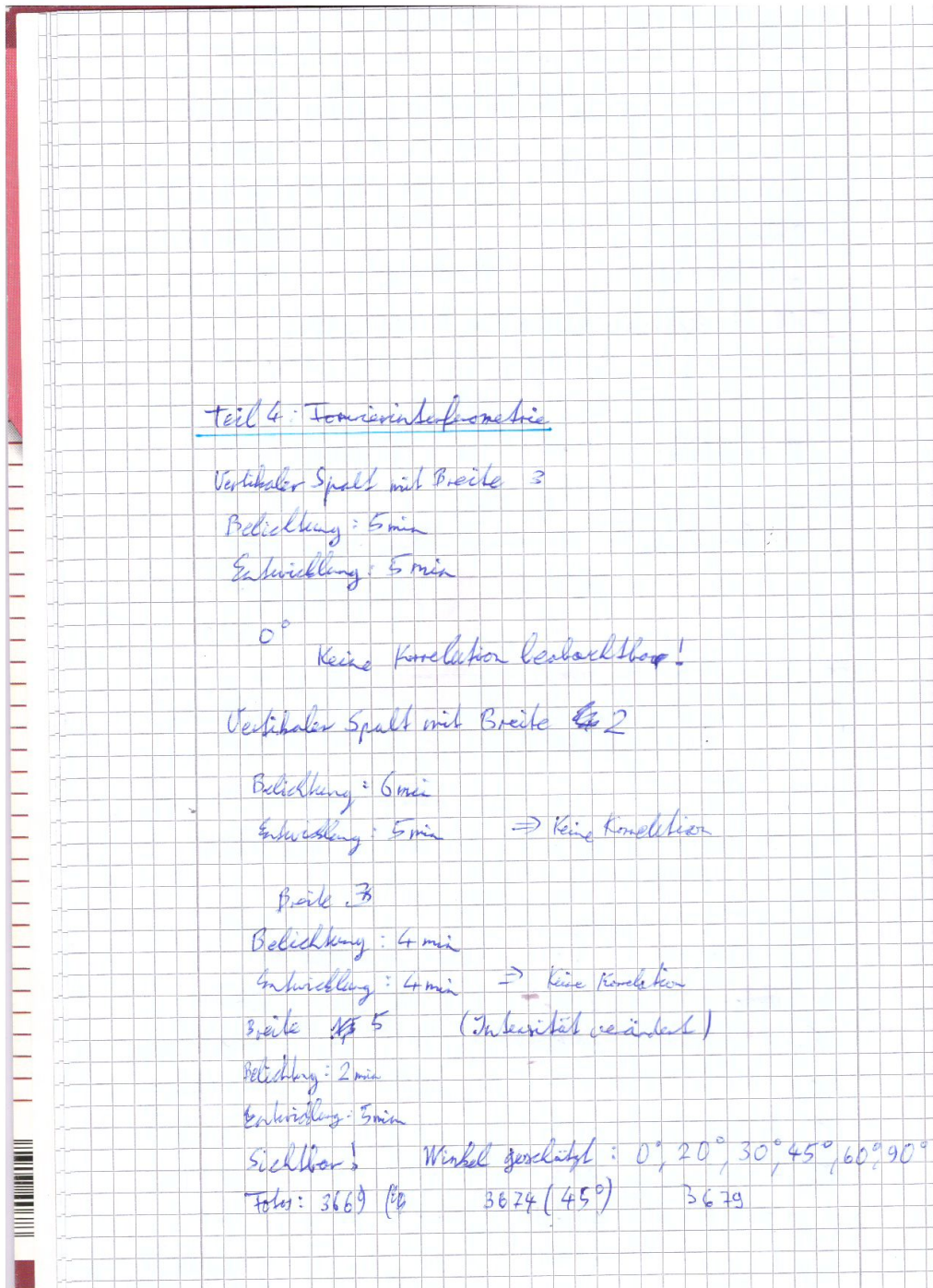


Figure 5.11: Laboratory journal entry page 8

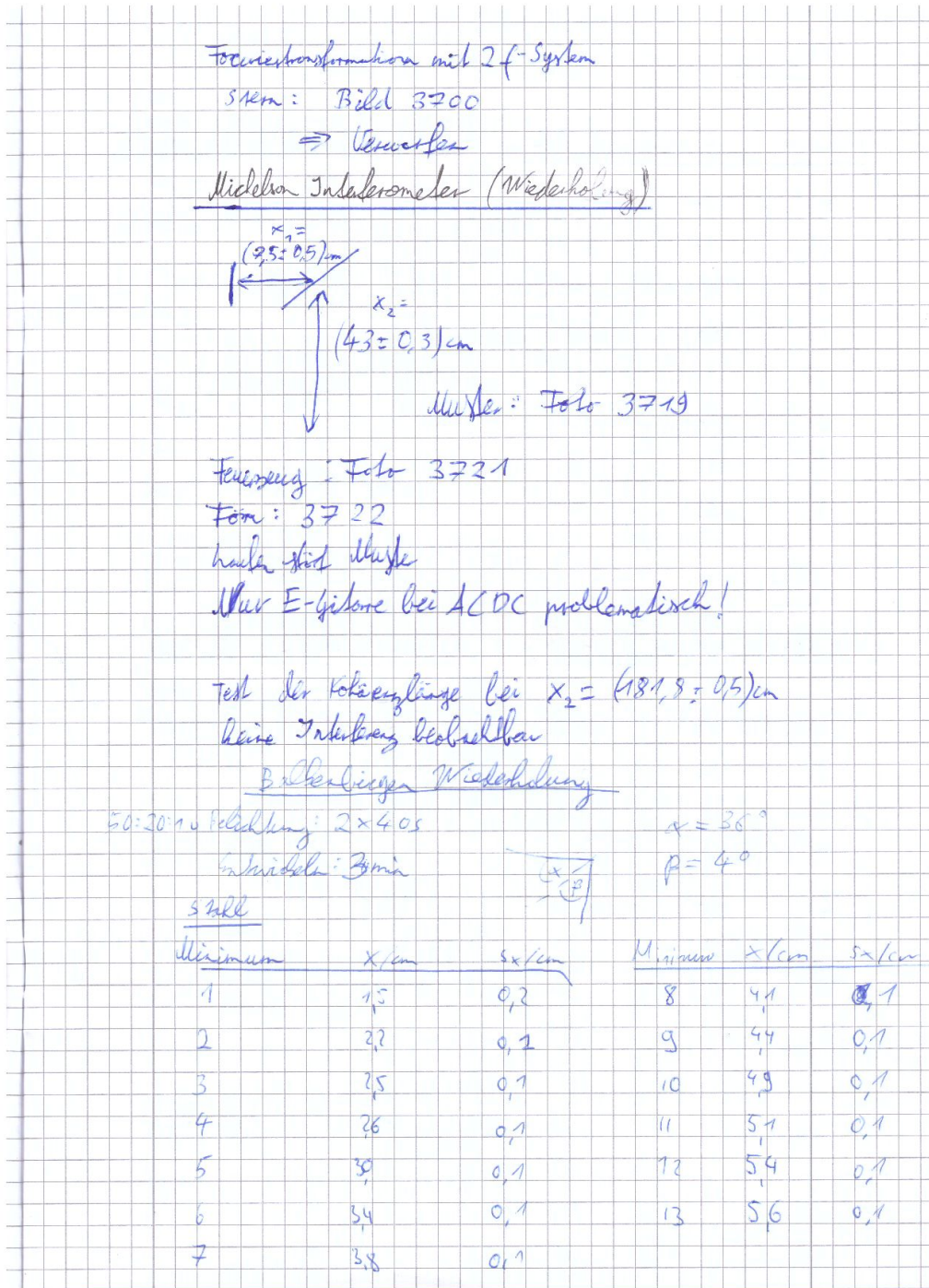


Figure 5.12: Laboratory journal entry page 9

<u>2 Messung:</u> 20 · 30 · 20					
<u>Stahl</u>					
keine Beobachtung möglich					
<u>Messring</u>					
Minimun	\bar{x} / cm	s_x / cm	Min	\bar{x} / cm	s_x / cm
1	0,8	0,2	11	4,8	"
2	1,3	0,2	12	5,0	"
3	1,7	0,1	13	5,3	"
4	2,0	"	14	5,5	"
5	2,4	"	15	5,2	"
6	2,8	"	16	5,9	"
7	3,1	"	17	6,2	"
8	3,5	"	18	6,4	"
9	3,8	"	19	6,8	"
10	4,3	"	20		
<u>Alu</u>					
Minimun	\bar{x} / cm	s_x / cm	Min	\bar{x} / cm	s_x / cm
1	0,2	0,2	11	4,2	"
2	0,2	0,2	12	4,4	"
3	1,3	0,1	13	4,7	"
4	1,6	"	14	5,7	"
5	2,0	"	15	5,4	"
6	2,4	"	16	5,6	"
7	2,7	"	17	5,8	"
8	3,2	"	18	6,2	"
9	3,5	"	19	6,4	"
10	3,7	"	20	6,8	"

Figure 5.13: Laboratory journal entry page 11

5.4 R Source code

```
1 graphics.off()
2 path = dirname(sys.frame(1)$ofile)
3
4 library(Hmisc)
5 library(pracma)
6
7 Es = c()
8
9 files = dir(path, pattern = ".csv$")
10
11 # constants
12 b = 10.5e-3 # Breite in meter
13 c = 5.05e-3 # Dicke in meter
14 L = 9.9
15 a = L / 2 / 100
16
17 mat_en = list("Alu" = "aluminium", "Stahl" = "steel", "Messing" = "brass")
18
19 # defining masses in Gramm
20 masse = list()
21 masse$alu1 = 20 # 1. Runde
22 masse$alu2 = 10 # 2. Runde
23 masse$alu3 = 10 # keine Interferenz vernünftig beobachtbar
24 masse$alu4 = 10 # keine Interferenz vernünftig beobachtbar Alu10_1.jpg
25 masse$alu5 = 20 # letzte Messreihe Alu20_1.jpg
26 masse$messing1 = 20 # 1. Runde
27 masse$messing2 = 20 # 2. Runde
28 masse$messing3 = 20 # letzte Donnerstag 1. Bild Messing 20_1.jpg
29 masse$messing4 = 20 # letzte Donnerstag 2. Bild Messing 20_2.jpg
30 masse$messing5 = 30 # letzte Donnerstag neue Masse Messing 30_1.jpg
31 masse$stahl1 = 20 # 1. Runde
32 masse$stahl2 = 50 # 2. Runde
33 masse$stahl3 = 50 # letzte Donnerstag 1. Bild Stahl50_1.jpg
34 masse$stahl4 = 50 # letzte Donnerstag 2. Bild Stahl50_2.jpg
35 masse$stahl5 = 20 # keine Interferenz vernünftig beobachtbar
36
37
38 alphas = deg2rad(c(40, 42, 36, 36, 46))
39 s_alpha = deg2rad(3)
40
41 betas = deg2rad(c(40, 8, 4, 4, 15))
42 s_beta = deg2rad(3)
43
44 lambda = 632.8e-9
45
46 # initializing outputfile
```

```
47 cat("material & m/g & $\\alpha$\\\\textdegree & $\\beta$\\\\textdegree & P1 & $s_{P1}$\$  
  & $\\chi^2_{red}$ & E/GPa & $s_E$/GPa\\\\\\n\\\\hline\\n", file = paste(path, "  
output.txt", sep = "/"))  
48  
49 for(file_ in files){  
50  
51   data_ = read.csv(paste(path, file_, sep = "/"), header = TRUE, as.is = TRUE,  
      sep = "\\t")  
52  
53  
54  
55   png(paste(path, gsub("\\.csv", ".png", file_), sep = "/"), width = 6,  
     height = 4, units = "in", res = 600)  
56   par("mar" = c(4, 4, 1, 1))  
57   par("oma" = c(0, 0, 0, 0))  
58  
59  
60   alpha = alphas[as.numeric(gsub(".*(\\d+).*", "\\\\[1", file_))]  
61   beta = betas[as.numeric(gsub(".*(\\d+).*", "\\\\[1", file_))]  
62  
63   material = sub("(.*\\\\d+.*", "\\\\[1", file_)  
64   material_en = mat_en[[material]]  
65   mass = masse[[tolower(sub(".csv", "", file_))]]  
66   F = mass / 1000 * 9.81  
67  
68   cat("\n", file_, "masse: ", mass, sep = "")  
69   flush.console()  
70  
71  
72   # calculating stuff  
73   x = data$x / 1000  
74   s_x = data$s_x / 1000  
75   y = (lambda / 4 * (2 * data$k+1)) / (cos(alpha) + cos(beta))  
76   s_y = sqrt((( lambda / 4 * (2 * data$k+1)) / (cos(alpha) + cos(beta))^2)^2  
    * ((sin(alpha)* s_alpha)^2 + (sin(beta) * s_beta)^2))  
77  
78   # fit durchführen  
79   dat = data.frame(x, y, s_x, s_y)  
80   fit = nls(  
81     y ~ P1 * ( (a * x^2 - x^3/6 ) ) + P2 * x + P3,  
82     data = dat,  
83     start = list(  
84       P1 = 0.01,  
85       P2 = 0.1,  
86       P3 = 0.1  
87     ),  
88     #weights = 1 / (s_x^2 + s_y^2),  
89     control = list(maxiter = 500)  
90   )
```

```

91
92
93     P1 = summary(fit)[[10]][1,1]
94     P2 = summary(fit)[[10]][2,1]
95     P3 = summary(fit)[[10]][3,1]
96
97     s_P1 = summary(fit)[[10]][1,2]
98     s_P2 = summary(fit)[[10]][2,2]
99     s_P3 = summary(fit)[[10]][3,2]
100
101    fx = function(x){
102        return(P1 * ( (a * x^2 - x^3/6) ) + P2 * x + P3)
103    }
104
105    # Chi  $\chi^2$ 
106    E_X =
107
108    (P1 * ( (2 * a * x - x^2/2) ) + P2 )^2*s_x
109
110    # ((P1 * ( (a * s_x^2 - s_x^3)/6 ) + P2 * s_x))^2
111    # E_X = sqrt((s_x/x)^2 + (s_y^2))
112    chi2 = sum((fx(x) - y)^2 / (E_X)) / (length(x)-3)*1000
113
114    # Elastizitätsmodul berechnen
115    E = ( 12 * F ) / ( P1 * b * c^3 )
116    s_E = abs((( 12 * F ) / ( P1^2 * b * c^3 )) * s_P1 )
117
118
119
120    # Plot erstellen
121    xlim = range(0, x)
122    ylim = range(0, y)
123    plot(dat[1:2], ylim = ylim, ylab = "y [m^-6]", xlim = xlim, xlab = "x [cm]",
124          pch = NA, axes = FALSE)
125    box()
126    axis(1, at = pretty(dat[[1]]), lab = pretty(dat[[1]]) * 1e2, las = 1)
127    axis(2, at = pretty(dat[[2]]), lab = pretty(dat[[2]]) * 1e6, las = 1)
128    abline(v = axTicks(1), h = axTicks(2), col = "#888888")
129
130    points(dat[1:2], pch = 4, col = "#0000B0")
131    arrows(dat$x - dat$s_x,dat$y, dat$x + dat$s_x, dat$y, code = 3, angle = 90,
132          length = 0.0175, col = "#0000B0")
133    arrows(dat$x, dat$y - dat$s_y, dat$x, dat$y + dat$s_y, code = 3, angle = 90,
134          length = 0.0175, col = "#0000B0")
135    curve(fx, add = TRUE, col = "#B00000", from = 0, to = par("usr")[2])
136
137
138    legend("topleft",
139          c(

```

```
137     as.expression(bquote(.(material_en)~"/"~.(mass)~g)),
138     as.expression(bquote(y == P1 %.% (.a) %.% x^2 - x^3/6 ) + P2
139       %.% x + P3)),
140     as.expression(bquote(P1: .(signif(P1, 4)) %+-% .(signif(s_P1,
141       4)))),
142     as.expression(bquote(P2: .(signif(P2, 4)) %+-% .(signif(s_P2,
143       4)))),
144     as.expression(bquote(P3: .(signif(P3, 4)) %+-% .(signif(s_P3,
145       4)))),
146     as.expression(bquote(chi[red]^2: .(signif(chi2, 4)))),
147     as.expression(bquote(E: (.(round(E*10^-9, 1)) %+-% .(round(s_E
148       *10^-9, 1)))~10^9*Pa))
149   ),
150   cex = .7
151 )
152
153 cat(
154   material_en, " & ",
155   mass," & ",
156   rad2deg(alpha), " & ",
157   rad2deg(beta), " & ",
158   signif(P1, 4), " & ", signif(s_P1, 4)," & ",
159   signif(chi2, 4), " & ",
160   round(E*10^-9, 2)," & ", round(s_E*10^-9, 2),"\\"\\\"\\n",
161
162   sep = "", file = paste(path, "output.txt", sep = "/"), append = TRUE)
163 dev.off()
164
165 cat("\n\tchi^2: ", chi2)
166 }
167 cat("\n\n")
```

6 List of Figures

1.1	Two-beam Interference	4
1.2	Coherence time τ_c of a wave packet	5
1.3	Plane wave coherence length	5
1.4	Wave packet with finite coherence length	5
1.5	Diffraction	6
1.6	Fourier pair Rect/Sinc	7
1.7	Visual comparison of convolution, cross-correlation and autocorrelation	8
1.8	Illustration of the convolution theorem	9
1.9	4f-Correlator	9
1.10	Schematic setup for holography	10
1.11	Setup for obtaining reconstructed images	11
1.12	Term diagram of a He-Ne-Lasers	13
1.13	Michelson interferometer	14
1.14	Airy disk	14
1.15	Polluted laser beam	14
2.1	Experimental set-up Michelson interferometer	16
2.2	Part 2/3: experimental set-up holography	17
2.3	Interference pattern of the beam deflection	18
2.4	Photoshop evaluation	18
2.5	Signals for the stroboscopic lighting	19
2.6	Experimental set-up for the cross-correlation measurement	20
3.1	Observed interference pattern with the Michelson interferometer	21
3.2	Deflection of metal beam	22
3.3	Aluminium, measurement 1	24
3.4	Aluminium, measurement 2	25
3.5	Brass, measurement 1	25
3.6	Brass, measurement 2	26
3.7	Steel, measurement 1	26
3.8	Steel, measurement 2	27
3.9	f_{00} mode of the plate (442 Hz)	28
3.10	f_{10} mode of the plate (1068 Hz)	28
3.11	f_{20} mode of the plate (1738 Hz)	29
3.12	f_{11} mode of the plate (2931 Hz)	29
3.13	f_{21} mode of the plate (4129 Hz)	30
3.14	f_{31} mode of the plate (5429 Hz)	30
3.15	Plot of experimental values and $x_{m\nu}^2$	31
3.16	Autocorrelation of slit	32
3.17	Cross correlation 10°	32
3.18	Cross correlation 20°	32
3.19	Cross correlation 30°	32
3.20	Cross correlation 45°	33
3.21	Cross correlation 60°	33
3.22	Cross correlation 80°	33
3.23	Cross correlation 90°	33
3.24	Comparison of experimental and simulated cross-correlation	34
5.1	Geometry of the beam deflection	37
5.2	Bessel functions of the first kind (Order 0-2)	39

5.3	Oscillations of the plate at resonant frequencies	40
5.4	Laboratory journal entry page 1	41
5.5	Laboratory journal entry page 2	42
5.6	Laboratory journal entry page 3	43
5.7	Laboratory journal entry page 4	44
5.8	Laboratory journal entry page 5	45
5.9	Laboratory journal entry page 6	46
5.10	Laboratory journal entry page 7	47
5.11	Laboratory journal entry page 8	48
5.12	Laboratory journal entry page 9	49
5.13	Laboratory journal entry page 11	50

7 List of Tables

1	Experimental data for the elastic moduli	23
2	Literature and experimental values for the obtained elasticity moduli	24
3	Literature and experimental values for the obtained resonant frequencies	31
4	Summary of experimental and literature values for the elastic moduli	35
5	Summary resonant frequencies	36
6	Calculated $x_{m\nu}$ values	38
7	Calculated resonant frequencies	39
8	Experimental resonant frequencies	39

8 Bibliography

- [1] Köhli, M., *Holographie*, Experimental Instructions, University Freiburg, Februar 2011
- [2] Unmüßig, S., *Ein Versuch zur holographischen Interferometrie*, Teacher's Thesis, University Freiburg, November 1995
- [3] Demtröder, W., *Experimentalphysik Band 2: Elektrizität und Optik*, Springer, 6th Auflage, 2012
- [4] Hecht, E., *Optik*, Oldenbourg, 5th Auflage, 2009
- [5] Goodman, J., *Introduction to Fourier Optics*, Oldenbourg, 2nd edition, 1996